energies

MDPI

Article

Finite z-Slice Fuzzy Speed Control of a DC Motor Using Hybrid HO-CPO Optimization

Nuri Alper Metin

Department of Electronics and Automation, Vocational School, Kırıkkale University, 71100 Kırıkkale, Turkey; nurialpermetin@kku.edu.tr

Abstract

Speed control of direct-current (DC) drives requires a balance between tracking performance and electrical demand. This study jointly optimizes controller gains, membership geometry, input uncertainty, three z-levels and their weights, and 25 rule consequents in a finite layered fuzzy controller, labeled T3 in the numerical records. A two-stage evaluation separates optimizer performance from controller-architecture comparisons. Stage I compares study-specific HO, CPO, and Hybrid HO-CPO procedures for the same controller, with 5050 objective evaluations per run. Across 20 matched runs, the hybrid achieves the lowest mean cost (107.5093), followed by CPO (114.8554) and HO (131.1904); rank-based tests identify significant differences. Stage II independently tunes T1, IT2, and finite T3 controllers using the same hybrid and evaluation budget. Their mean costs are 106.2192, 104.6669, and 104.6439, respectively, with no significant architecture difference (Friedman $p = 0.7047$). Tests with parameter variation, measurement noise, alternative operating conditions, reduced inductance, and perturbed objective weights show that the preferred controller depends on the metric and scenario. The layered controller is competitive in simulation, although its small mean-cost advantage over IT2 is accompanied by a longer optimization time.

Keywords: DC motor drive; speed control; layered fuzzy control; Hybrid HO-CPO; equal-budget optimization; robustness analysis; fuzzy architecture benchmark

1. Introduction

Armature-controlled direct-current (DC) motors are used in positioning systems, conveyors, laboratory drives, and low- to medium-power automation. Their electrical and mechanical dynamics can be described through the relationships among armature voltage, current, electromagnetic torque, and shaft speed. Speed regulation becomes more demanding when reference changes coincide with load disturbances and actuator limits. A controller must recover promptly while keeping current and voltage demand acceptable across operating points. Proportional–integral–derivative control remains a standard benchmark, and population-based optimization provides a practical way to tune nonlinear controllers [1–3]. Recent studies in *Energies* have examined fuzzy and nonlinear control for transient regulation and disturbance rejection in AC and permanent-magnet drives [4,5].

Fuzzy control offers a rule-based approach when plant uncertainty or changes in operating conditions limit the usefulness of one fixed linear tuning. Its foundations include Type-1 sets, Mamdani inference, adaptive and model-based schemes, and Type-2 formulations [6–14]. In motor drives, speed error and error rate can be mapped directly to

Check for updates

Academic Editor: Sid Ahmed El Mehdi Ardjoun

Received: 3 September 2026
Revised: 16 October 2026
Accepted: 17 October 2026
Published: 23 October 2026

Copyright: © 2026 by the author. Licensee MDPI, Basel, Switzerland. This article is an open access article distributed under the terms and conditions of the Creative Commons Attribution (CC BY) license.

a control action, while membership parameters describe the location and uncertainty of linguistic boundaries.

Studies on DC motor drives have examined fuzzy PI/PID, adaptive fuzzy, neuro-fuzzy, and particle-swarm-tuned controllers, including simulation and hardware-oriented implementations with field-current coordination and FPGA realization [15–22]. Many of these designs, however, tune gains or a limited subset of membership parameters while leaving the rule table and uncertainty structure fixed.

Type-3 fuzzy systems introduce an additional membership level beyond Type-2 systems, with reported applications in robotic manipulators, induction-motor drives, and nonlinear dynamic systems [23–29]. A separate line of work uses finite zSlices to represent general Type-2 sets. These concepts require different mathematical definitions; increasing the number of interval layers alone does not establish a Type-3 system.

This work formulates DC speed regulation as a joint controller-tuning problem. Scaling gains, integral action, membership geometry, input uncertainty, three z-levels and their weights, and the 25 rule consequents form a 61-variable decision vector. The finite layered controller is labeled T3 in the experimental records. Study-specific HO- and CPO-inspired procedures and their hybrid search this common representation. The evaluation first compares the optimizers for a fixed architecture, then compares independently tuned T1, IT2, and layered controllers under a common optimizer and evaluation budget.

1.1. Related Work on Fuzzy Motor-Drive Control

Type-2 control research includes stability analysis, systematic design, and evolutionary tuning [30–36]. Recent motor-drive applications include hybrid metaheuristic tuning, fuzzy PMSM and BLDC control, PSO-assisted adaptation, and interval Type-2 control on embedded hardware [37–41].

Recent electric-drive research has also developed along complementary directions that are relevant to the present optimization study. Jin et al. proposed a zero-speed sensorless PMSM scheme that combines virtual-flux signal injection with a hybrid active-flux observer, addressing observability and stable operation in the low-speed region [42]. Cheng et al. combined radial-basis-function modeling and ADALINE adaptation for harmonic estimation and suppression in PMSM drives, showing how a hybrid intelligent estimator can be embedded in the drive-control loop [43]. Chen et al. examined dq-axis current distribution and control of a negative-salient PMSM for vehicle applications, paying particular attention to machine-specific operating characteristics and transient behavior [44]. Wang et al. coupled parameter-sensitivity analysis with multiobjective optimization in an electromechanical design problem, illustrating how sensitivity information can be used to interpret and guide optimized solutions [45]. Although these studies concern different machines and control objectives, they provide useful contemporary context for observer design, intelligent compensation, transient control, and sensitivity-aware optimization.

Higher-order fuzzy applications use different membership hierarchies and inference operators [23–29]. Their performance must therefore be interpreted in relation to the implemented controller and validation conditions. Section 2.1.3 defines the finite layered construction evaluated here.

Many motor-drive studies use Type-1 fuzzy, fuzzy-PID, or interval Type-2 controllers. Fuzzy and PSO-assisted designs have improved speed regulation relative to the conventional or manually tuned controllers used in their respective tests [15–20]. Related studies cover DC and BLDC motors, induction motors, and motor-pump systems [41,46–50]. Optimization often targets gains, scaling factors, or selected membership parameters. Joint optimization of the complete rule base, antecedent uncertainty, layer parameters, and output centers has received less attention in this application.

Evolutionary and hybrid metaheuristic approaches have been used to tune fuzzy-controller parameters and structures [24,25,33], including motor-drive applications [37,40,46]. The original Crested Porcupine Optimizer (CPO) and Hippopotamus Optimization (HO) are population-based search methods [51,52]. The present study uses simplified update schemes inspired by these methods. Its optimizer comparisons, therefore, concern the implementations defined in Section 2.3, rather than an independent benchmark of the canonical algorithms.

Table 1 compares the scope of selected theoretical and applied studies. Section 4.4 provide numerical context while retaining the differences in plant models and test conditions.

Table 1. Selected studies relevant to the scope of the present work.

Study	System/Method	Main Contribution	Difference from the Present Scope
Karnik et al. [8]	Type-2 fuzzy logic systems	Established Type-2 system structure and inference	Theoretical framework without the present DC-drive tuning study.
Liang and Mendel [9]	Interval Type-2 fuzzy logic systems	Developed interval Type-2 theory and design principles	Does not address joint DC-drive controller optimization.
Rahmani et al. [17]	PSO-tuned DC motor FLC	Optimized a fuzzy speed controller using PSO	Uses fewer tunable components than the present joint parameter search.
Kumbasar and Hagras [35]	zSlices-based general Type-2 fuzzy PI controller	Developed a self-tuning general Type-2 fuzzy PI controller	Uses a PI structure with a different tuning formulation.
Chatzipapas and Karnavas [41]	Embedded IT2-PID DC micro-motor control	Tested online PSO tuning under hardware resource constraints	Uses an IT2-PID architecture and an embedded validation platform.
Younus et al. [37]	Hybrid GWO-PI BLDC control	Tuned speed regulation under load and reference changes	Optimizes PI gains rather than fuzzy memberships and rule entries.
Castillo and Melin [23]	Type-3 fuzzy control approach	Presented a control-oriented Type-3 formulation	Does not provide the present DC-drive benchmark.
Amiri et al. [52]	Hippopotamus Optimization (HO)	Introduced a population-based optimization method	General-purpose optimizer without the present controller formulation.
Abdel-Basset et al. [51]	Crested Porcupine Optimizer (CPO)	Introduced a nature-inspired optimization method	General-purpose optimizer without the present controller formulation.
Bal [29]	Type-3 fuzzy robust speed control	Studied indirect vector control of an induction motor	Uses a different motor and control structure.
Ghamari et al. [46]	Adaptive BLDC control with HIL validation	Combined adaptive control, optimization, and HIL testing	Uses a different controller family and validation framework.

Research Gap

The study addresses joint parameter optimization and controlled evaluation. Earlier motor-control work commonly tunes gains or selected membership parameters [15–22,27–29,37–41,46–50]. Here, the decision vector includes the gains, all membership centers, input uncertainty coefficients, layer parameters, and 25 rule consequents. Stage I compares search procedures for the same layered controller. Stage II compares independently optimized architectures using one optimizer and one evaluation budget.

Within the broader literature, the present contribution is positioned as an optimization-centered controller co-design study for an armature-controlled DC motor. It does not seek to replace PMSM-specific sensorless observers, harmonic-compensation schemes, or dq-axis current-control strategies. Instead, it examines whether controller gains, membership geometry, uncertainty parameters, layer variables, and the rule base can be tuned

jointly while keeping optimizer comparison and controller-architecture comparison under explicitly controlled evaluation budgets.

1.2. Main Contributions

The main contribution is a mixed continuous-discrete formulation for jointly tuning 61 controller variables, evaluated through separate optimizer and architecture comparisons. An initial experiment evaluates the intensified hybrid under unequal evaluation effort. Stage I assigns 5050 evaluations to each search procedure for the same layered controller. Stage II applies the same hybrid, plant, objective, and budget to T1, IT2, and finite T3 controllers. Further tests examine parameter variation, noise, an alternative reference/load profile, current protection, inductance, and objective weights.

2. Materials and Methods

The closed-loop system consists of an armature-controlled DC motor, a finite layered fuzzy speed controller, integral action, and voltage-command conditioning. The motor model retains the armature resistance and inductance, torque and back-EMF constants, rotor inertia, viscous friction, and applied load torque. A 1 ms sampling interval is used over 3.2 s. The reference and load schedules test acceleration, deceleration, and disturbance recovery, while the objective monitors both tracking and electrical demand.

Speed error and filtered error rate are the controller inputs. Each normalized input is described by five triangular sets: negative big (NB), negative small (NS), zero (Z), positive small (PS), and positive big (PB). Five optimized consequent centers define the output levels. The Type-1 fuzzy logic controller (T1 FLC) uses deterministic membership grades; the IT2 scheme adds upper and lower antecedent memberships; and the finite T3 scheme evaluates three interval layers at optimized z-levels. All three use a complete 5×5 rule base [7–14,30–36,53].

The controller is tested with a multistep reference and scheduled load-torque changes. A first-order filter smooths the error derivative, and a bounded integral state limits error accumulation. The fuzzy correction is attenuated near the reference. Feedforward, fuzzy, and integral terms are added to form the voltage command, which is subject to a rate limit and amplitude bounds.

The derivative-filter coefficient is 0.92, the integral-state bound is ± 150, and the integral contribution uses $\tanh(0.035\, I)$, where I is the accumulated error. Input normalization uses $\tanh(G_e\, e)$ and $\tanh(G_{de}\, de_f)$, with de_f denoting the filtered error rate. The fuzzy correction is multiplied by $0.40 + 0.60 \min(1, |e|/18)$. The feedforward voltage is $R(B\, \omega_{ref} + T_L)/K_t + K_b\, \omega_{ref}$. Table 2 lists the nominal voltage and voltage-increment limits.

Table 2. Simulation settings and driving constraints.

Quantity	Symbol	Value	Unit	Description
Sampling time	T_s	1×10^{-3}	s	Integration step and controller update period.
Total simulation time	t_{end}	3.2	s	Duration of each simulated trajectory.
Maximum armature voltage	V_{max}	220	V	Upper bound of the unipolar armature command.
Nominal current threshold	I_{lim}	35	A	Soft-penalty threshold; hard protection is tested separately.
Maximum voltage increment	ΔU_{max}	10.0	V/step	Nominal voltage change allowed per sampling step.

The initial experiment uses HO, CPO, and an intensified HO-CPO hybrid with a population of 50 and 100 outer iterations. The hybrid combines preliminary elite information, additional trial generation, local refinement, an archive, and restarts. That configuration does not equalize the number of objective evaluations. Stage I and Stage II use separate

protocols with 5050 evaluations per procedure, including initialization. The results from the two protocols are reported separately.

Candidate controllers are evaluated using tracking error, residual error, overshoot, voltage variation, current-threshold violations, and residual oscillation. The objective for Stage I and Stage II also includes a plateau-tracking term, defined in Section 2.5.1. A quadratic penalty discourages a current above 35 A; the nominal experiments do not impose hard-current saturation. Tracking is additionally summarized by root-mean-square error (RMSE). Cost distributions from 20 runs are compared with Friedman and Iman–Davenport tests, followed by Holm-adjusted Wilcoxon tests when the omnibus result is significant. MATLAB-2023b performs the simulation, optimization, statistical analysis, and output generation.

Figure 1 shows the workflow from decision-vector encoding to closed-loop simulation and statistical evaluation. Controller performance is assessed together with current demand and the voltage constraints.

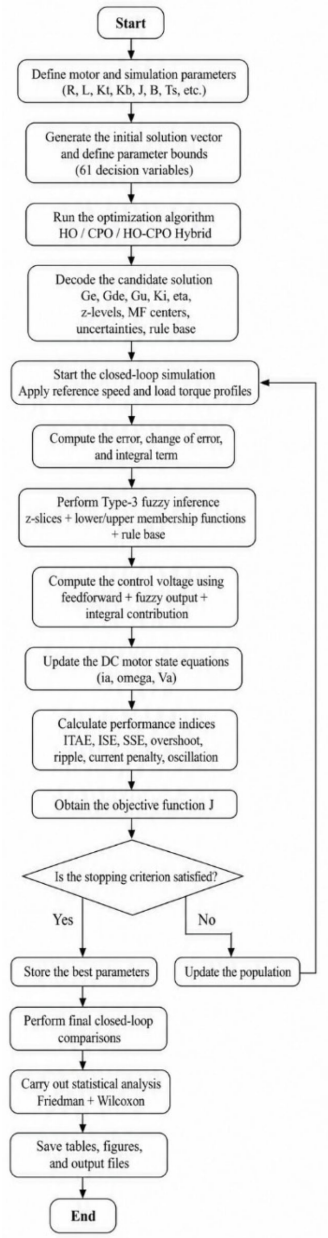


Figure 1. Overall workflow for fuzzy-controller co-design and DC motor performance assessment.

2.1. Fuzzy Controller Architectures

2.1.1. Type-1 Fuzzy Logic Controller

A Type-1 fuzzy set A on a universe X assigns a single membership grade $\mu_A(x) \in [0, 1]$ to each input x [10,12,14]. The present controller uses five triangular sets for speed error and error rate, together with five output-center values. The optimizer adjusts their centers and overlap. This representation keeps the input partitions and selected consequent levels directly interpretable.

For rule R_{ij}, IF e is A_i AND Δe is B_j THEN u is C_r, the firing strength is the minimum of the two antecedent grades. The output is the firing-strength-weighted average of the selected consequent centers. It is a center-weighted inference scheme rather than the centroid of an aggregated Mamdani output area [12,13]. Gains G_e, G_{de}, and G_u scale the input and output channels, and integral action is added outside the fuzzy map. The denominator is bounded below by 10^{-9}; when every rule has zero activation, the fuzzy output is zero.

The Type-1 rule base and membership centers are optimized independently under the common plant, objective, population, and evaluation budget. The comparison therefore concerns complete optimized architectures, including their different active search dimensions.

2.1.2. Interval Type-2 Fuzzy Logic Controller

Interval Type-2 fuzzy logic extends the Type-1 description by allowing the primary membership grade itself to occupy an interval. An interval Type-2 set is therefore represented by an upper membership function (UMF) and a lower membership function (LMF); the region between them is the footprint of uncertainty (FOU). This representation is widely used when the location or width of a linguistic boundary cannot be regarded as exact. The basic operations, upper/lower membership representation, and control interpretation of interval Type-2 systems are established in the Type-2 fuzzy literature [7–9,11,30,32–36,54,55].

In the IT2 baseline, the optimized centers define the upper triangular membership functions. Each input set has an uncertainty coefficient that contracts its lower triangle about the same apex. Lower and upper rule strengths are calculated with the minimum t-norm and combined as $\eta w_U + (1 - \eta) w_L$. Their weighted consequent-center average gives the output, with a denominator floor of 10^{-9}. This implementation uses a blending approximation and does not perform iterative type reduction.

Uncertainty is confined to the antecedents. The error and error-rate sets have optimized upper and lower memberships, whereas each rule selects a crisp consequent from five optimized output centers. No output-side uncertainty coefficient is included in the decision vector. The coincident output curves visualize the center locations and have a zero-width footprint of uncertainty; inference uses the centers rather than the area of an aggregated output set [9,11,30,31,34–36,54–58].

2.1.3. Finite z-Slice Layered Controller

Formal Type-3 systems require an additional membership hierarchy [23,26,53,59–61]. The α-plane and zSlices studies cited here describe Type-2 representations [54–58]. The present implementation instead constructs three interval layers at optimized z-levels and averages their outputs. The label T3 identifies this finite layered architecture in the numerical records; it does not imply equivalence to a general Type-3 inference or type-reduction operator.

Equation (1) denotes the finite set of layers, where A_{zl} is the interval description at level z_l. The positive aggregation coefficients β_l in Equation (5) are optimized separately

and normalized to sum to one. The finite layer representation follows the z-slice concept used for general Type-2 systems [57,58].

$$\widetilde{A} = \sum_{\ell=1}^{L} z_\ell / \widetilde{A}_{z_\ell}, 0 < z_1 < z_2 < \ldots < z_L \leq 1 \quad (1)$$

Figure 2 illustrates the layered construction. The horizontal axis is the primary universe, the z-axis identifies the discrete layers, and the vertical axis is membership grade. Each layer contains upper and lower triangular membership functions. The connecting surfaces are visual interpolation; inference only uses the three optimized z-levels.

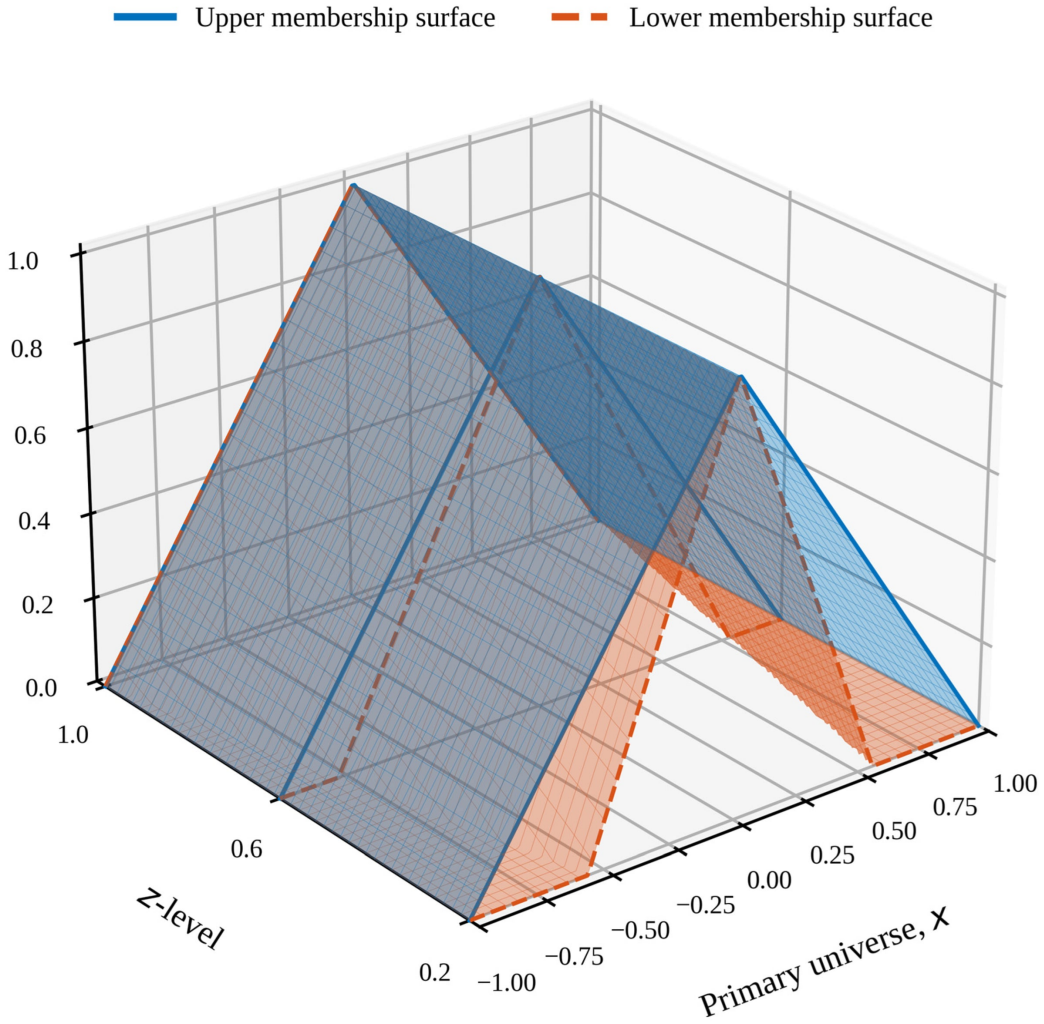


Figure 2. Finite interval-layer construction used in the controller labeled T3. Connecting surfaces visualize the relationships among the discrete z-slices.

Equation (2) defines the upper triangular membership function, with support limits a and c and apex b. For an interior set, the support limits are the adjacent optimized centers; the outer limits of the first and last sets are -1 and 1. The membership grade is zero at the support endpoints.

$$\mu^U(x) = \begin{cases} 0, & x \leq a, \\ \dfrac{x-a}{b-a}, & a < x \leq b, \\ \dfrac{c-x}{c-b}, & b < x < c, \\ 0, & x \geq c \end{cases} \quad (2)$$

Equation (3) defines the lower triangle. For input-set uncertainty δ_i and layer z_l, the code uses $\rho_{il} = \max(0.20, 1 - \delta_i(1 - z_l))$, $a_{il}{}^L = b_i - \rho_{il}(b_i - a_i)$, and $c_{il}{}^L = b_i + \rho_{il}(c_i - b_i)$. The lower support is therefore nested within the upper support. The IT2 baseline uses the same construction at $z = 0$.

$$\mu_\ell^L(x) = \begin{cases} 0, & x \le a_\ell^L, \\ \dfrac{x - a_\ell^L}{b - a_\ell^L}, & a_\ell^L < x \le b, \\ \dfrac{c_\ell^L - x}{c_\ell^L - b}, & b < x < c_\ell^L, \\ 0, & x \ge c_\ell^L \end{cases} \tag{3}$$

Equation (4) first calculates lower and upper rule strengths using the minimum t-norm, then blends them with η. The same blending convention is used by the IT2 and finite T3 implementations.

$$\begin{aligned} w_{ij}^l = \eta\ min\left(\mu_{E,i}^{U,l}(e),\ \mu_{\Delta E,j}^{U,l}(\Delta e)\right) \\ +(1-\eta)\ min\left(\mu_{E,i}^{L,l}(e),\ \mu_{\Delta E,j}^{L,l}(\Delta e)\right) \end{aligned} \tag{4}$$

In Equation (5), each layer is normalized separately to obtain y_l, and the final output is the weighted average of these layer outputs. The consequent $c_r(i,j)$ is selected from the shared output-center vector, β_l is the normalized positive layer weight, and $\varepsilon = 10^{-9}$. The result is clipped to $[-1, 1]$. A layer with no active rules contributes zero.

$$\begin{aligned} y_l = \frac{\sum_{i,j} w_{ij}^l c_{r(i,j)}}{max\left(\varepsilon,\ \sum_{i,j} w_{ij}^l\right)} \\ u = \sum_{l=1}^{3} \beta_l y_l,\ \sum_{l=1}^{3} \beta_l = 1 \end{aligned} \tag{5}$$

Equations (1)–(5) define the finite layered calculation used in Stage I and Stage II. Its tunable quantities are the membership centers, input uncertainty coefficients, z-levels, layer weights, and rule consequents. The T3 label identifies this implementation throughout the reported results.

2.1.4. Computational Hierarchy and Limiting Cases

Each optimized z-level defines an interval footprint. Across layers, both the interval geometry and the aggregation contribution may change. If all layers coincide, the architecture reduces to a single interval-layer form; if every upper and lower membership pair also coincides, it becomes Type-1-like [9,11,57,58].

These are limiting relations within the numerical architecture. The independently optimized T1, IT2, and finite T3 experiments in Section 3.3 compare complete designs under a common optimizer and evaluation budget. Differences include their active parameter dimensions and tuned rule maps, so the experiment does not isolate uncertainty order as a single causal factor.

2.2. Armature-Controlled DC Motor Model

The armature-controlled DC motor is represented by the coupled electrical and mechanical equations of motion [62–66]. Armature current i_a and angular speed ω are the state variables, armature voltage v_a is the control input, and load torque T_L is treated as an external disturbance. Equation (6) balances the applied voltage against the resistive,

inductive, and back-EMF terms and Equation (7) balances electromagnetic torque against viscous friction, inertia, and load torque.

$$V_a(t) = R\, i_a(t) + L\, \frac{di_a(t)}{dt} + K_b\, \omega(t) \tag{6}$$

$$J\, \frac{d\omega(t)}{dt} = K_t\, i_a(t) - B\, \omega(t) - T_L(t) \tag{7}$$

Here, R and L are armature resistance and inductance, K_b is the back-EMF constant, K_t is the torque constant, J is rotor inertia, and B is the viscous friction coefficient [62–71].

Equations (8) and (9) give the electrical and mechanical derivatives used in the simulation [65–71].

$$\frac{di_a}{dt} = \frac{-R\, i_a - K_b\, \omega + V_a}{L} \tag{8}$$

$$\frac{d\omega}{dt} = \frac{K_t\, i_a - B\, \omega - T_L}{J} \tag{9}$$

Forward Euler integration advances both states with the sampling period T_s. The current update uses the voltage command at step k and the current and speed from step k−1. The mechanical update uses the previous current; negative computed speed is clipped to zero. Equations (10) and (11) give the recursions [65–70].

$$i_a(k) = i_a(k-1) + T_s\, \frac{di_a}{dt} \tag{10}$$

$$\omega(k) = max\left(0,\ \omega(k-1) + T_s \frac{K_t i_a(k-1) - B\omega(k-1) - T_L(k)}{J}\right) \tag{11}$$

The model provides current and speed trajectories for evaluating the controller. It excludes converter switching, magnetic saturation, commutation, and other hardware effects [62–71]. The results therefore describe the stated simulation model.

2.3. Optimization and Evaluation Protocol

The three search procedures use the same bounded 61-variable representation and scalar objective. HO and CPO denote the study-specific updates below, inspired by the original methods [51,52]. Related hybrid and memetic methods provide context for combining search operators [72–79]. The comparisons assess the implementations defined below.

2.3.1. HO-Inspired Search Procedure

The HO-inspired procedure combines attraction to the current best solution, the mean of the five best candidates, and a decaying uniform perturbation, as shown in Equation (12) [52].

$$\mathrm{x}_i^{t+1} = \mathrm{x}_i^t + \alpha_t\, \mathrm{r}_1 \odot \left(\mathrm{x}_{best}^t - \mathrm{x}_i^t\right) + \beta\, \mathrm{r}_2 \odot \left(\mathrm{x}_{mean}^t - \mathrm{x}_i^t\right) + \gamma_t\, \mathrm{u} \odot (\mathrm{ub} - \mathrm{lb}) \tag{12}$$

In the equal-budget procedure, progress is q = FE/MaxFEs, with FE denoting the evaluations used so far. The coefficients in Equation (12) are $\alpha_t = 0.85(1 - q)$, $\beta = 0.35$, and $\gamma_t = 0.04(1 - q)$. The vectors r_1 and r_2 are uniform on [0, 1], and u is uniform on [−1, 1].

Each trial is projected onto the variable bounds, structurally repaired, evaluated, and only retained if it improves the incumbent.

Algorithm 1 summarizes this update and selection cycle.

Algorithm 1. HO-inspired search

Step	Procedure
1	Initialization: initialize a population X of N candidates randomly within [LB, UB].
2	Evaluation: evaluate the fitness f(X) of all candidates.
3	Selection: identify the current best solution x_{best}.
4	While the stopping criterion is not satisfied
5	Ranking: rank the population according to fitness.
6	Elite mean: calculate the mean vector of the elite solutions.
7	For each candidate x_i
8	Generate a trial solution using Equation (12).
9	Boundary control: apply [LB, UB] and repair infeasible variables.
10	Evaluation: evaluate the trial fitness.
11	If the trial fitness is better than $f(x_i)$
12	Replace x_i with the trial solution.
13	End if
14	End for
15	Update the global best solution x_{best}.
16	End while

2.3.2. CPO-Inspired Search Procedure

The CPO-inspired procedure assigns candidates to an exploratory or contracted update according to their current rank [51]. Equations (13) and (14) give the two updates.

$$x_i^{t+1} = x_i^t + \lambda_1 r_3 \odot \left(x_{best}^t - x_i^t\right) + \lambda_2 r_4 \odot \left(x_p^t - x_q^t\right) + \sigma_t n \tag{13}$$

The exploratory update uses $\lambda_1 = 0.70$ and $\lambda_2 = 0.45$. At progress q, the active group contains max(4, round(max(0.35, $1 - q$)N_{pop})) candidates from the top of the ranked population. Both update modes add Gaussian noise scaled elementwise by $(0.025 + 0.02(1 - q))(ub - lb)$.

$$x_i^{t+1} = \eta_1 x_i^t + \eta_2 x_{best}^t + \eta_3 x_r^t + \sigma_t n \tag{14}$$

The contracted update uses $\eta_1 = 0.50$, $\eta_2 = 0.35$, and $\eta_3 = 0.15$; x_r is an auxiliary peer. Every proposal is repaired and evaluated before greedy acceptance.

The two modes retain the same decision vector definition and feasibility repair.

Algorithm 2 summarizes the implemented CPO cycle: mode assignment, trial generation, repair, objective evaluation, greedy replacement, and best-solution update.

Algorithm 2. CPO-inspired search

Step	Procedure
1	Initialization: initialize the population X within [LB, UB].
2	Evaluation: evaluate f(X) for all candidates.
3	Selection: identify the initial best solution x_{best}.
4	While the stopping criterion is not satisfied
5	Ranking: rank the population according to fitness.
6	Ratio calculation: compute the active search ratio.
7	For each candidate x_i
8	If x_i belongs to the active group
9	Generate a trial solution using Equation (13).
10	Else
11	Generate a trial solution using Equation (14).
12	End if
13	Boundary handling: apply [LB, UB] and repair infeasible variables.
14	Evaluation: evaluate the generated trial solution.
15	If the trial fitness is better than $f(x_i)$
16	Replace x_i with the trial solution.
17	End if
18	End for
19	Update x_{best} and record the convergence history.
20	End while
21	Return x_{best} and the convergence history.

2.3.3. Intensified HO-CPO Hybrid

The intensified hybrid in the initial experiment generates several trial moves for each candidate. Its HO-oriented displacement is defined in Equation (15).

$$\Delta_H = r_1 \odot (x_{best} - x_i) + r_2 \odot (x_{mean} - x_i) \tag{15}$$

The corresponding CPO-oriented displacement is given in Equation (16).

$$\Delta_C = r_3 \odot (x_p - x_q) + r_4 \odot (x_{best} - x_i) \tag{16}$$

An elite-centered local move is added through Equation (17).

$$\Delta_L = r_5 \odot (x_{elite} - x_i) + r_6 \odot (x_{best} - x_{2nd}) \tag{17}$$

The weighted fused move is given in Equation (18).

$$x_F^{t+1} = x_i^t + \alpha_t \Delta_H + \beta_t \Delta_C + \gamma_t \Delta_L + \Sigma_t n \tag{18}$$

Equations (15)–(18) summarize the combination of HO-oriented, CPO-oriented, local, and fused moves in the intensified hybrid. Their weights vary with progress and recent improvement [72,74,78]. The equal-budget hybrid uses the separate operator-selection procedure described in Section 2.5.1.

The intensified hybrid maintains an archive, preserves elite solutions, performs local refinement, and restarts weak candidates after stagnation. Its initial population includes elites from completed standalone HO and CPO searches. It can also evaluate several trials for one population member. Its effective evaluation effort is therefore greater than that of

the standalone procedures, and the experiment measures the performance of the complete configured search [72,74,78].

Algorithm 3 summarizes the intensified procedure. The equal-budget hybrid described in Section 2.5 starts from a shared initial population, without incorporating solutions from completed standalone searches.

Algorithm 3. Initial intensified HO-CPO hybrid

Step	Procedure
1	Hybrid initialization: form the population from elite HO and CPO candidates, mixed candidates, and repaired random solutions.
2	Evaluation and archiving: evaluate the initial population and create an archive of high-quality solutions.
3	Selection: determine the initial global best solution x_{best}.
4	while the stopping criterion is not satisfied
5	Adaptive weighting: compute weights for HO-based moves, CPO-based moves, and local exploitation.
6	For each candidate x_i
7	Multi-strategy trial generation: generate an HO-oriented trial using Equation (15).
8	Generate a CPO-oriented trial using Equation (16).
9	Generate a local elite trial using Equation (17).
10	Generate a fused trial using Equation (18).
11	Trial selection: retain the best-performing candidate among the generated trials.
12	Variable repair: apply bounds and repair continuous and discrete variables.
13	Evaluation: evaluate the repaired trial solution.
14	If the trial fitness is better than $f(x_i)$
15	Replace x_i with the selected trial solution.
16	End if
17	End for
18	Refinement: apply elite jittering and local search around selected high-quality candidates.
19	Global update: update the archive and x_{best}.
20	If stagnation is detected
21	Restart the weakest portion of the population to maintain diversity.
22	End if
23	End while

2.4. Statistical Comparison

Rank-based tests compare the procedures over 20 trial blocks [80,81]. In Stage I and Stage II, each block shares an initial unit-hypercube population, while update streams use separate recorded seeds. The blocks represent repeated stochastic runs on one control problem, rather than independent plants or datasets [82,83]. Statistical inference is therefore restricted to this optimization setup.

After ranking the procedures within each block, the mean rank assigned to algorithm j is used to calculate the Friedman statistic in Equation (19).

$$\chi_F^2 = \frac{12N}{k(k+1)} \sum_{j=1}^{k} \overline{R}_j^2 - 3N(k+1) \tag{19}$$

Here, N = 20 is the number of blocks, k = 3 is the number of procedures, and $\overline{R}_j$ is the mean within-block rank of procedure j. Rejection of the Friedman null indicates an overall rank difference without identifying a particular pair [80].

Because the chi-square approximation can be conservative with small or moderate samples, the Friedman statistic is supplemented by the Iman–Davenport transformation in Equation (20).

$$F_F = \frac{(N-1)\chi_F^2}{N(k-1)-\chi_F^2} \tag{20}$$

Under the null, Equation (20) is compared with an F distribution with k − 1 and (k − 1)(N − 1) degrees of freedom [81].

If the omnibus test is significant, paired procedures are compared with the Wilcoxon signed-rank test. For block i, the paired difference is defined in Equation (21).

$$d_i = x_i - y_i \tag{21}$$

Zero paired differences are omitted and the remaining absolute differences are ranked. T+ and T− denote the positive and negative rank sums used in Equation (22) [84,85]. Stage I *p*-values are calculated using the two-sided normal approximation without continuity correction.

$$W = \min(T^+, T^-) \tag{22}$$

The signed-rank statistic uses both the direction and ranked magnitude of the paired differences. Its interpretation assumes an appropriate symmetric distribution of paired differences [84,86].

For the three pairwise contrasts, Holm's sequential adjustment controls the familywise Type I error rate at 0.05 [87]. The smallest ordered *p*-value is first multiplied by three, the second by two, and the third by one; cumulative maxima enforce monotonic adjusted *p*-values, capped at one.

Omnibus testing precedes the Holm-adjusted pairwise comparisons [82,87,88]. The tests assess run-level differences within the stated experiment. They neither correct unequal evaluation effort nor establish superiority over other control problems.

2.5. Equal-Budget Evaluation Protocol

2.5.1. Evaluation Stages and Implementation Settings

The equal-budget protocol separates optimizer performance from controller-architecture comparisons. Stage I compares the three optimizers for a fixed layered architecture, with 5050 objective evaluations each. Stage II applies the selected hybrid to independently tuned T1, IT2, and finite T3 controllers under the same budget.

Stage I uses a population of 50. Within each matched block, one unit-hypercube population is mapped to the common 61-variable space. The vector contains G_e, G_{de}, G_u, K_i, η, three z-levels, three layer weights, five centers and five uncertainty coefficients for each input, five consequent centers, and 25 integer rule entries. The proposal bounds are $G_e \in [0.002, 0.050]$, $G_{de} \in [0.0001, 0.008]$, $G_u \in [1, 80]$, $K_i \in [0, 25]$, $\eta \in [0.10, 0.90]$, $z_1 \in [0.10, 0.40]$, $z_2 \in [0.35, 0.75]$, $z_3 \in [0.70, 1.00]$, and layer weights in [0.10, 3.00]. Membership-center proposal bounds are [−1, 1], uncertainty coefficients lie in [0, 0.60], and rule entries are rounded to {1, 2, 3, 4, 5}. Repair sorts and spaces the centers within [−0.95, 0.95], with a minimum gap of 0.12. The joint z-level repair imposes a minimum gap of 0.08 within [0.15, 0.95] and may shift individual levels from their proposal intervals.

The equal-budget hybrid normally uses the same CPO update as the standalone procedure. For each candidate, an alternative operator is selected with probability 0.08 when no stagnation is recorded, 0.18 after one stagnant cycle, and min(0.35, 0.18 + 0.06 s) for $s \geq 2$

stagnant cycles. Depending on rank and progress, the alternative is an HO-oriented move, a fused move, or local refinement. The archive retains up to eight distinct solutions, and the elite mean uses the five best population members. After eight cycles without a global-best improvement greater than 10^{-10}, restart proposals target max(1, round(0.05 N_{pop})) weak candidates, which is three for N_{pop} = 50. Initialization, all trial evaluations, and restarts count toward the 5050-evaluation limit. The remaining coefficients are given in runHybridEqualBudget (doi.org/10.5281/zenodo.23536636). The configuration fields restartFrac = 0.22 and localTrialsPerCycle = 4 are inactive; the restart and refinement behavior follows the procedure described above.

The objective for Stage I and Stage II augments the initial objective with a plateau-tracking term. This term penalizes residual error near the end of every nonzero reference segment, including the intermediate plateau. Equation (23) gives the objective used in Stage I and Stage II.

$$J = ITAE + 0.02ISE + 10E_{ss} + 12E_{pl} + 0.10P_{os} + 0.08P_{rip} + P_{cur} + 3P_{osc} \quad (23)$$

ITAE and ISE are rectangular sample sums of $t|e|$ and e^2 multiplied by T_s. E_{ss} is the mean absolute error over the final n_{tail} = max(10, round(0.20N)) samples, where N is the number of time samples. E_{pl} averages the late-segment mean absolute errors: for a nonzero segment of n samples, averaging starts floor(0.60n) samples after its first sample. P_{os} is T_s $\Sigma\max(\omega - \omega_{ref},0)^2$. P_{rip} = T_s $\Sigma|v_a[k] - v_a[k-1]|$ retains the scaling used in the code. P_{cur} = 250 T_s $\Sigma\max(|i_a[k]| - 35, 0)^2$, and P_{osc} is half the sample standard deviation of e[k] for $t \geq 0.25$ s. The weights are fixed engineering coefficients with the units implied by these definitions. Section 3.5.3 examines their sensitivity by re-scoring fixed controllers under named weight sets and 100 random ± 25% perturbations.

2.5.2. Stage I: Matched Equal-Budget Optimizer Protocol

Stage I uses 20 matched runs. Each block shares an initial population, while the stochastic update streams use independent recorded seeds. Friedman and Iman–Davenport tests provide omnibus comparisons; significant results are followed by Holm-adjusted Wilcoxon signed-rank contrasts [80,81,84,87]. Optimizer selection uses the full cost distribution. The separately seeded illustrative run uses initial-population seed 111 and update seeds 211, 311, and 411 for HO, CPO, and Hybrid HO-CPO. It is not a median-selected member of the 20-run experiment. Elapsed optimization time is recorded as a secondary measure.

2.5.3. Stage II Controller-Architecture Benchmark

Stage II independently optimizes T1, IT2, and finite T3 architectures using the same hybrid procedure, nominal plant, objective, population size, and 5050-evaluation budget. Common variables are G_e, G_{de}, G_u, K_i, 15 membership centers, and all 25 rule consequents. The gain bounds are [0.002, 0.050], [0.0001, 0.008], [1, 80], and [0, 25], respectively. Membership centers initially have box bounds $[-1, 1]$; after repair, they lie within $[-0.95, 0.95]$ with at least 0.12 separation. Consequents are integers in {1, . . ., 5}. The benchmark measures the outcome of optimizing each specified architecture, including their different search dimensions.

T1 has 44 active variables, with zero uncertainty and inactive layer variables. IT2 has 55 active variables, adding η and ten input uncertainty coefficients. Finite T3 activates all 61 variables, including the three z-levels and their weights. Neither IT2 nor finite T3 has an independent output-uncertainty vector. All architectures use the same center-ordering repair, but their search dimensions, tuned gains, and rule maps differ.

2.5.4. Robustness and Sensitivity Tests

Robustness tests use the representative controllers without retuning. They cover independent uniform ± 20% changes in R, L, K_t, K_b, J, and B; zero-mean speed-measurement noise with standard deviation 0.50 rad/s; an alternative reference/load profile; and a combined scenario. Each stochastic scenario has 50 realizations per architecture. Different random streams are used for T1, IT2, and T3, so the Monte Carlo comparisons are descriptive rather than paired by disturbance realizations. The simulation also recalculates feedforward using the perturbed plant parameters. These tests therefore assess parameter variation with parameter-aware feedforward, rather than unknown plant mismatch with fixed nominal feedforward.

For the alternative profile, speed commands change to 90, 140, 70, and 105 rad/s at 0.08, 0.95, 2.05, and 2.75 s, respectively, starting from zero. Load torque is initially 0.18 N·m and changes to 0.32, 0.27, 0.36, and 0.20 N·m at 0.55, 1.45, 2.25, and 2.85 s. The combined scenario uses this profile with parameter variation and measurement noise.

The hard-current test projects the proposed voltage onto the interval that satisfies $|i_a[k]| \leq 35$ A under the one-step Euler model, intersected with [0, 220] V. Its bounds are $v_\pm = L(\pm I_{lim} - i_a[k-1])/T_s + R\, i_a[k-1] + K_b\, \omega[k-1]$. If the interval is empty, the code retains the amplitude-limited command, so the current bound is not guaranteed in that case. Projection follows the nominal voltage-rate limit and can override that rate limit when active. The nominal comparison in Section 3.5.1 does not activate this projection.

The sensitivity analyses are used to qualify the interpretation of a selected optimum rather than to claim universal robustness. They test whether conclusions based on a fixed controller are strongly dependent on plant parameters or objective weighting. This use is consistent with sensitivity-guided optimization, in which the influence of design variables and assumptions is examined before an optimum is interpreted as practically meaningful [45].

3. Results

3.1. Initial Experiment with Unequal Evaluation Budgets

3.1.1. Search Space, Constraints, and Composite Objective

Table 3 lists the nominal motor parameters. Resistance and inductance set the electrical time scale, the torque and back-EMF constants couple current and speed, and inertia and friction determine the mechanical response.

Table 3. Parameters of the armature-controlled DC motor model.

Parameter	Symbol	Value	Unit	Description
Armature resistance	R	2.0	Ω	Electrical resistance of the armature circuit.
Armature inductance	L	0.5	H	Armature inductance governing current dynamics.
Torque constant	K_t	0.50	N·m/A	Torque produced per unit of armature current.
Back-EMF constant	K_b	0.50	V/(rad/s)	Back-EMF generated per unit of angular speed.
Moment of inertia	J	0.020	kg·m^2	Rotor inertia governing mechanical acceleration.
Viscous friction coefficient	B	0.12	N·m·s/rad	Coefficient of speed-dependent viscous torque.

Table 2 lists the simulation and actuator settings. Each run lasts 3.2 s with a 1 ms sampling interval. The nominal armature command lies between 0 and 220 V and changes by at most 10 V per sample. Current above 35 A is penalized in the objective. Hard-current protection is evaluated separately in Section 3.5.1.

Table 4 summarizes the initial search settings and the 61-variable representation. It includes four gains, three z-levels, three layer weights, 15 membership centers, ten input

uncertainty coefficients, η, and 25 rule consequents. The active settings of the equal-budget hybrid are given in Section 2.5.1.

Table 4. Initial optimization settings and decision-variable structure.

Item	Value or Range	Description
Procedures	HO, CPO, intensified HO-CPO hybrid	Initial procedures with unequal evaluation effort
Total number of decision variables	61	Total number of optimized controller parameters
Population size	50	Nominal population size used by all three procedures
Number of HO iterations	100	Outer iterations used by HO
Number of CPO iterations	100	Outer iterations used by CPO
Number of hybrid iterations	100	Outer iterations used by the intensified hybrid procedure
Number of elite individuals	4	Elite setting of the initial intensified procedure.
Local search iterations	20	Additional local-search iterations in the initial procedure
Restart fraction	0.22	Restart setting of the initial experiment; Stage I uses the setting in Section 2.5.1
Stagnation window	8	Stagnation window in cycles
Error scaling factor	[0.002, 0.050]	Input gain applied to the speed error
Change-of-error scaling factor	[0.0001, 0.008]	Input gain applied to the error derivative
Output scaling factor	[1.0, 80.0]	Output gain of the fuzzy controller
Integral gain	[0.0, 25.0]	Gain associated with the integral action
Blending coefficient	[0.10, 0.90]	Mixing coefficient between lower and upper membership responses
z-level locations	[0.10, 0.40], [0.35, 0.75], [0.70, 1.00]	Bounds assigned to the three z-level positions
z-level weights	[0.10, 3.00]	Weight interval defined for each z-level
Error MF centers	[−1.0, 1.0]	Bounds of the five error membership-function centers
Error MF uncertainty	[0.00, 0.60]	Bounds of the five uncertainty values for the error MFs
Change-of-error MF centers	[−1.0, 1.0]	Bounds of the five change-of-error membership-function centers
Change-of-error MF uncertainty	[0.00, 0.60]	Bounds of the five uncertainty values for the change-of-error MFs
Output MF centers	[−1.0, 1.0]	Bounds of the five output membership-function centers
Rule base	[1, 5]	Discrete index interval used for the 25 fuzzy rules

The initial experiment and the equal-budget experiments use different objective definitions. The tail-error measure Ess denotes mean absolute error over the final samples. Stage I and Stage II use the plateau-aware objective in Equation (23). Costs from the initial and equal-budget experiments must therefore be interpreted within their respective protocols, rather than as direct improvements over one another.

Figure 3 shows convergence in the initial intensified-search experiment. The hybrid begins from a stronger population because it incorporates elite information from the preceding standalone searches and then improves further through additional trial generation and local refinement. The horizontal axis is therefore outer iteration, not an equalized

function-evaluation count; search efficiency under matched evaluation effort is assessed separately in Section 3.2.

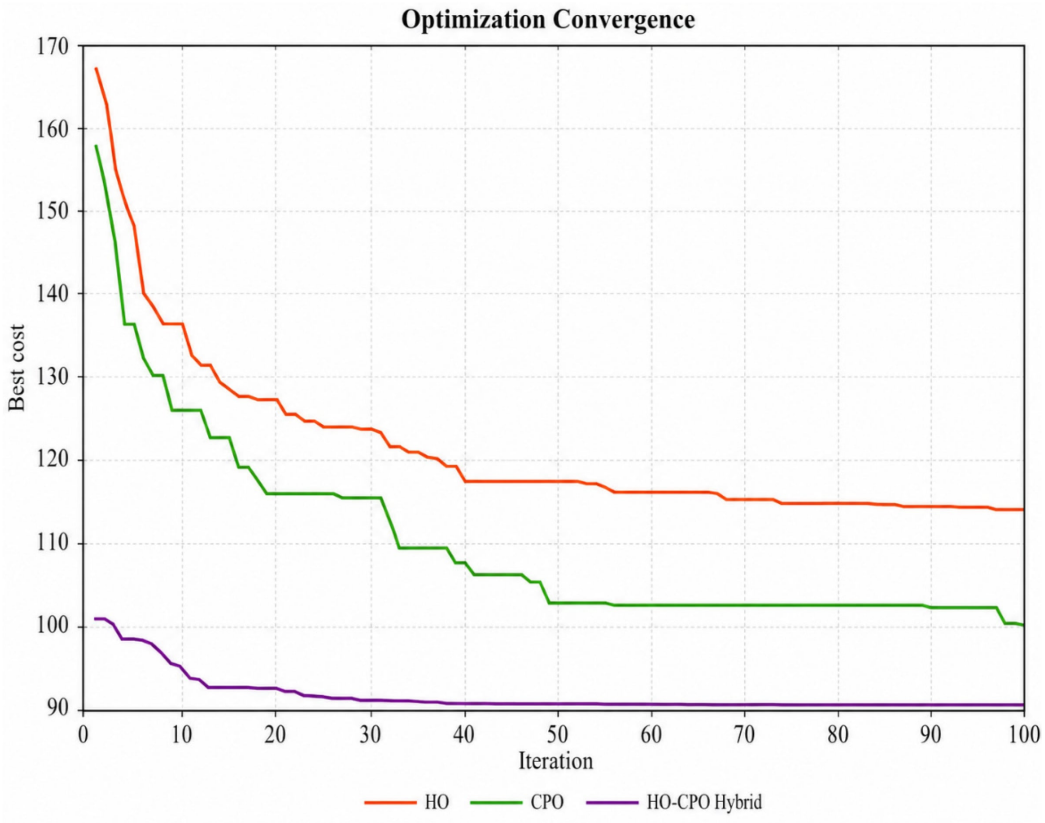


Figure 3. Best objective value over outer iterations for HO, CPO, and HO-CPO (evaluation budgets are unequal).

3.1.2. Optimized Finite T3 Membership and Rule Structures

Table 5 lists the optimized parameters from the initial experiment. Figures 4–6 show the resulting error, error-rate, and consequent partitions for the three procedures.

Table 5. Optimized finite T3 parameter values obtained in the complete-framework experiment.

Parameter	HO	CPO	Hybrid HO-CPO
G_e	0.02781	0.04214	0.04177
G_{de}	0.00403	0.00246	0.00237
G_u	56.25094	77.77925	80.00000
K_i	0.15140	11.43121	11.00091
η	0.43870	0.18770	0.19675
z-levels	[0.28333, 0.51928, 0.84811]	[0.18689, 0.52152, 0.72275]	[0.18596, 0.51101, 0.72470]
z-weights	[1.10518, 1.36558, 0.87900]	[0.98735, 1.98204, 2.02861]	[1.02232, 1.89546, 2.00237]
Error MF centers	[−0.67046, −0.11655, 0.28308, 0.52016, 0.81674]	[−0.75670, −0.07261, 0.04739, 0.72242, 0.89748]	[−0.85931, −0.06756, 0.05322, 0.69606, 0.86540]
Error MF uncertainty	[0.38408, 0.53684, 0.30645, 0.30967, 0.38776]	[0.28200, 0.22970, 0.23024, 0.40176, 0.17958]	[0.27743, 0.22795, 0.23827, 0.40106, 0.17705]
Error-rate MF centers	[−0.47196, −0.07937, 0.23333, 0.76055, 0.90621]	[−0.90716, −0.64907, −0.05999, 0.37470, 0.91112]	[−0.89849, −0.63728, −0.07991, 0.35494, 0.89142]

Table 5. *Cont.*

Parameter	HO	CPO	Hybrid HO-CPO
Error-rate MF uncertainty	[0.23407, 0.07525, 0.30287, 0.13527, 0.30413]	[0.08110, 0.26070, 0.34745, 0.21183, 0.13178]	[0.08771, 0.26533, 0.34645, 0.20804, 0.12535]
Output MF centers	[−0.92057, −0.67017, −0.00337, 0.74733, 0.87340]	[−0.95000, −0.42040, 0.03251, 0.49628, 0.94996]	[−0.95000, −0.47983, 0.00864, 0.47501, 0.94982]
Rule consequents	25 optimized integer entries; see Table 6	25 optimized integer entries; see Table 7	25 optimized integer entries; see Table 8

The HO rule table is non-monotonic (Table 6). Zero and small negative consequents dominate its first row, while several central and positive error-rate combinations select positive actions. The optimized table therefore differs from a conventional symmetric rule map.

Table 6. Fuzzy rule base obtained with HO.

dE/E	E_{NB}	E_{NS}	E_{Z}	E_{PS}	E_{PB}
dE_{NB}	Z	NS	NS	NS	Z
dE_{NS}	NB	NS	PS	PS	Z
dE_{Z}	Z	PS	PS	Z	PB
dE_{PS}	Z	Z	PS	NB	PS
dE_{PB}	PS	Z	NS	PS	PS

CPO assigns negative-big consequents to most combinations in the strongly negative error-rate row (Table 7). Zero actions dominate much of the central region, while positive-big outputs occur in selected positive-error combinations.

Table 7. Fuzzy rule base obtained with CPO.

dE/E	E_{NB}	E_{NS}	E_{Z}	E_{PS}	E_{PB}
dE_{NB}	NB	NB	NB	NB	Z
dE_{NS}	Z	Z	NB	PB	PB
dE_{Z}	NS	NS	Z	Z	Z
dE_{PS}	Z	Z	Z	Z	PS
dE_{PB}	Z	PB	PB	NS	PS

Table 8 gives the hybrid rule base. Its asymmetric entries act together with the optimized gains and the membership geometry.The gains, memberships, and rule tables show that each procedure converged to a different controller configuration.

Table 8. Fuzzy rule base obtained with the HO-CPO hybrid.

dE/E	E_{NB}	E_{NS}	E_{Z}	E_{PS}	E_{PB}
dE_{NB}	NB	NB	NB	NB	NS
dE_{NS}	PB	NB	NB	PB	PB
dE_{Z}	NS	NB	Z	PB	PS
dE_{PS}	NB	Z	Z	PB	PB
dE_{PB}	Z	PB	PB	PB	PB

Figure 4 shows the error membership structures reconstructed from the parameter sets in Table 5. Each controller is evaluated at its three optimized z-levels; the connecting surfaces are visualization only.

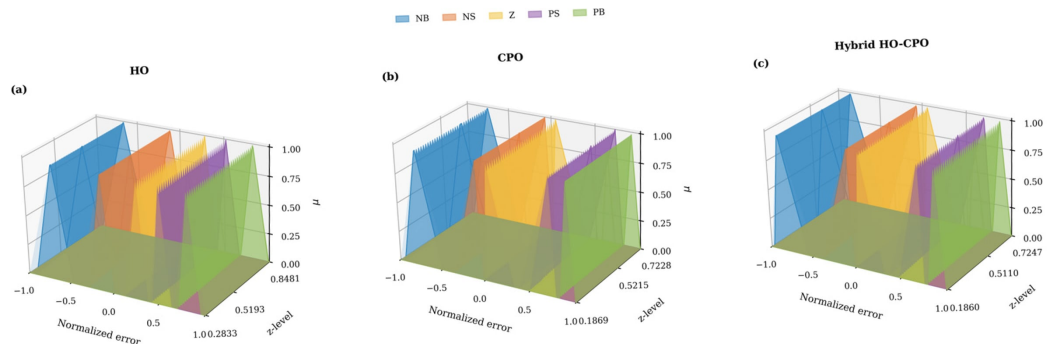


Figure 4. Three-dimensional z-slice speed-error membership structures obtained in the complete-framework experiment: (**a**) HO; (**b**) CPO; (**c**) Hybrid HO-CPO.

Figure 5 shows the corresponding error-rate membership structures. The centers, uncertainty coefficients, and z-levels are those of the HO, CPO, and hybrid solutions from the initial experiment.

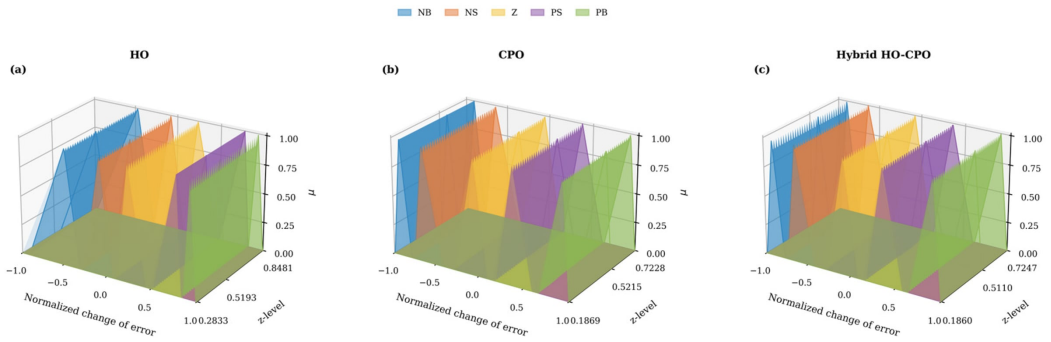


Figure 5. Three-dimensional z-slice change-of-error membership structures obtained in the complete-framework experiment: (**a**) HO; (**b**) CPO; (**c**) Hybrid HO-CPO.

Figure 6 shows the optimized consequent partitions. No output-side uncertainty vector is optimized, so the same partition is repeated across each controller's z-levels. Layer-dependent control action arises from the antecedent activations and aggregation weights.

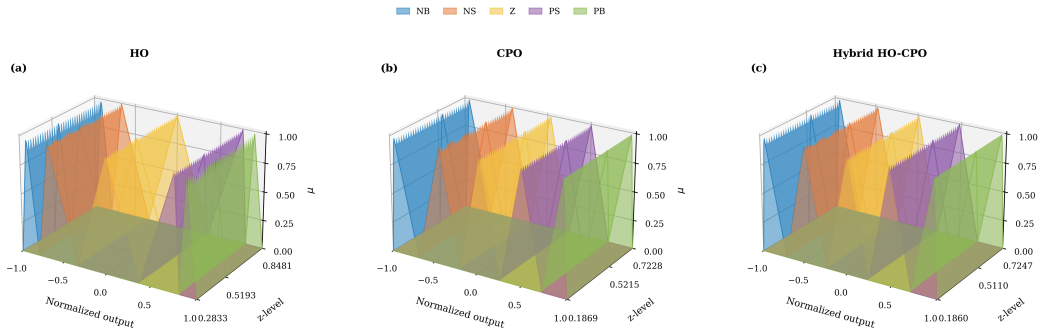


Figure 6. Optimized output membership structures obtained in the complete framework experiment: (**a**) HO; (**b**) CPO; (**c**) Hybrid HO-CPO. The consequent partition is shared across z-levels in the implemented model.

HO produced a smaller integral gain and a lower output gain than CPO and the hybrid. The hybrid reached the upper bound of G_u, while its z-levels and layer weights remained close to the CPO values. Differences in membership centers, input uncertainty, and rule entries produced distinct controller maps.

3.1.3. Closed-Loop Tracking and Electrical Response

Figure 7 shows the nominal profile. The reference is 0 rad/s before 0.1 s, 100 rad/s from 0.1 to 1.2 s, 130 rad/s from 1.2 to 2.2 s, and 80 rad/s thereafter. The load torque is 0.15 N·m before 0.8 s, 0.25 N·m from 0.8 to 1.8 s, 0.22 N·m from 1.8 to 2.4 s, and 0.18 N·m thereafter. The alternative-profile robustness scenario uses a different schedule.

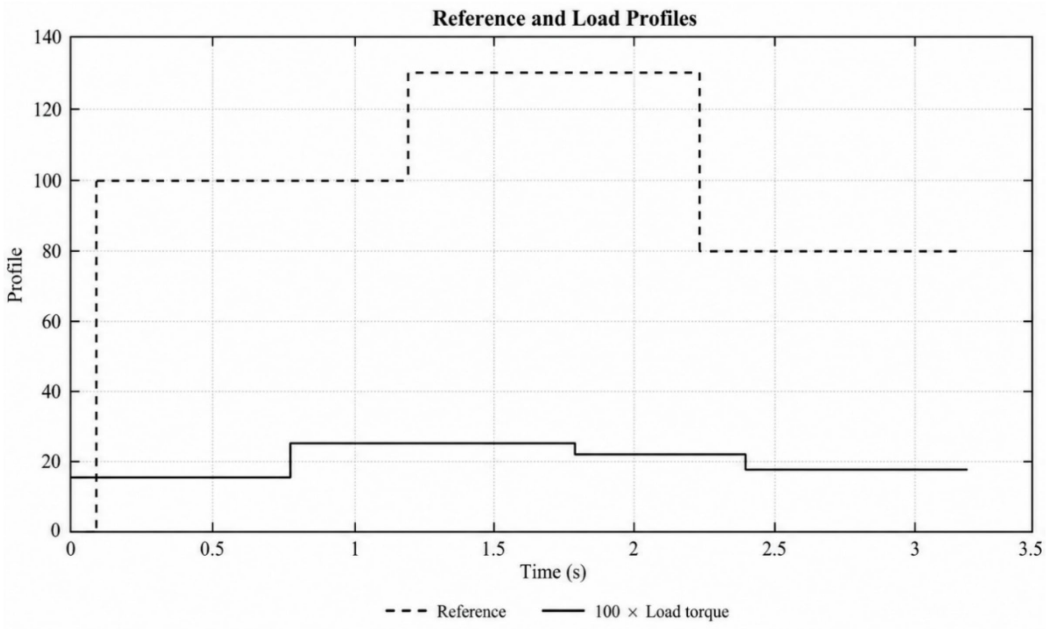


Figure 7. Nominal reference-speed and load-torque profiles.

Figure 8 compares speed trajectories from the initial experiment. The hybrid reaches the commanded regions rapidly and settles with smaller excursions than the selected CPO solution, while HO responds more gradually. Tables 9 and 10 quantify these responses alongside residual error and electrical demand.

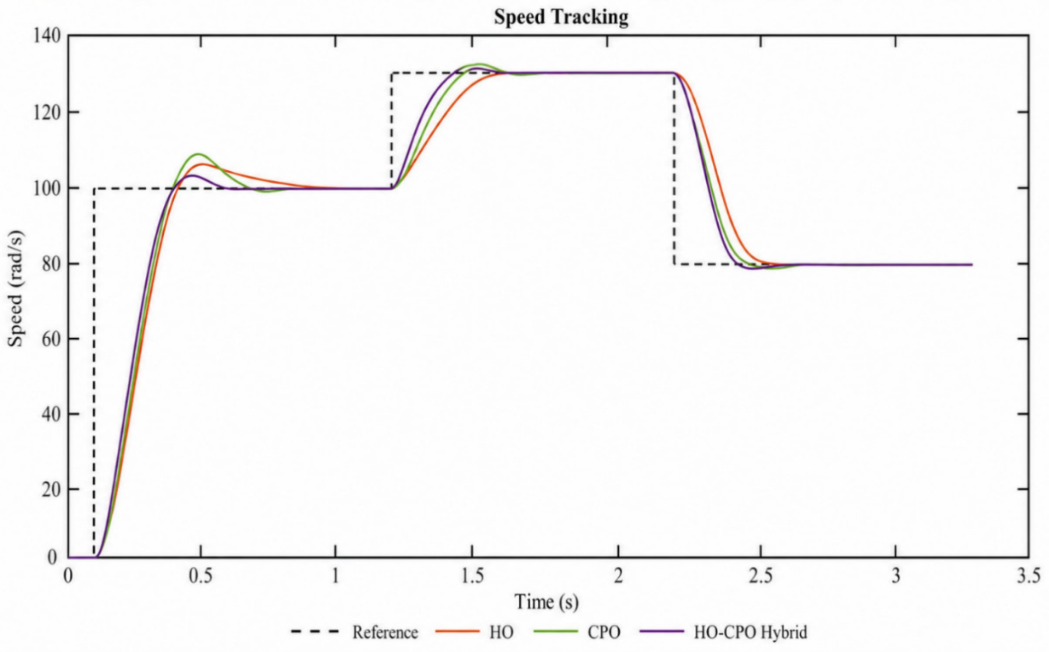


Figure 8. DC motor speed responses under the HO-, CPO-, and HO-CPO-tuned fuzzy controllers.

Table 9. Performance components for the selected HO, CPO, and HO-CPO hybrid solutions.

Algorithm	Cost	ITAE	Tail Error (rad/s)	Peak Current (A)	Overshoot-Related Penalty
HO	114.6055	29.4080	0.0122	34.1584	50.0094
CPO	101.1277	24.6585	0.2223	34.9159	49.9658
HO-CPO Hybrid	90.9662	21.7810	0.0195	35.0842	50.1435

Table 10. Time-domain performance of the selected solutions from the initial experiment.

Metric	HO	CPO	Hybrid HO-CPO
Cost	114.6055	101.1277	90.9662
ITAE	29.4080	24.6585	21.7810
RMSE (rad/s)	23.0036	22.1002	21.2247
Tail error (rad/s)	0.0122	0.2223	0.0195
Mean rise (s)	0.211	0.176	0.165
Mean settling (s)	0.434	0.380	0.325
Max overshoot (%)	6.285	8.711	3.967
Peak current (A)	34.1584	34.9159	35.0842

Figure 9 shows the associated armature currents. The largest differences occur during reference transitions. The intensified hybrid reaches 35.0842 A, exceeding the soft threshold by 0.0842 A, while the reported HO and CPO solutions remain below it. Current approaches similar operating levels after the transients. The faster response therefore entails a small penalized current excursion.

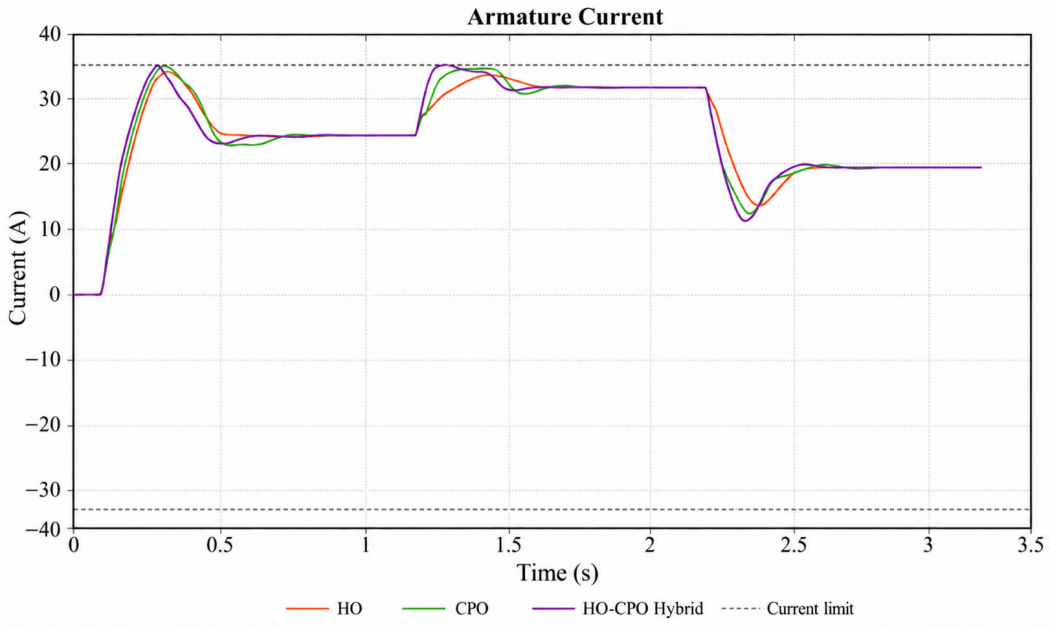


Figure 9. Armature-current responses under the three controllers (35 A denotes the soft-penalty threshold).

3.1.4. Performance and Repeated-Run Results

Table 9 presents the objective components from the initial experiment. The hybrid has the lowest cost (90.9662) and ITAE (21.7810), HO has the smallest tail-error indicator, and CPO has the smallest overshoot penalty. The hybrid also has the largest peak current (35.0842 A). Its lower cost reflects the chosen weighting of these quantities. Ess denotes the mean absolute tail error; Stage I and Stage II also report ISE separately.

Table 10 reports additional time-domain measures for the solutions from the initial experiment. The matching source and time series needed to reproduce these metrics are not included in the Supplementary Materials for Stage I and Stage II.

Note: All values refer to the selected controllers from the initial experiment. The time-domain measures include RMSE, 10–90% rise time, 2% settling time, and transition overshoot. The reported speed peaks are 130.038 rad/s at 1.867 s for HO, 131.847 rad/s at 1.518 s for CPO, and 131.190 rad/s at 1.491 s for the hybrid.

The time-domain metrics give the hybrid the shortest mean rise and settling times and the lowest RMSE. Its maximum transition overshoot is also smaller than that of the selected HO and CPO solutions. CPO is faster than HO but has greater overshoot. These results describe the procedures configured for the initial experiment, including the hybrid's 35.0842 A current peak and the additional evaluation effort.

Table 11 lists the 20 run-level costs from the initial experiment. The hybrid is lowest in every block, while the ordering of HO and CPO changes across runs. This result supports the complete intensified procedure under the settings of the initial experiment; it does not isolate search efficiency under equal evaluation effort.

Table 11. Objective values from 20 matched trials.

Run	HO	CPO	HO-CPO Hybrid	Lowest-Cost Procedure
1	126.0481	101.8897	80.1941	HO-CPO Hybrid
2	119.5947	114.8080	78.8135	HO-CPO Hybrid
3	114.4439	101.6182	89.2574	HO-CPO Hybrid
4	121.9009	116.2931	99.0212	HO-CPO Hybrid
5	111.5940	118.4899	90.6523	HO-CPO Hybrid
6	119.3697	108.7949	77.3025	HO-CPO Hybrid
7	132.4563	90.7216	68.4176	HO-CPO Hybrid
8	131.3526	116.5831	98.3386	HO-CPO Hybrid
9	130.6757	100.7946	84.6964	HO-CPO Hybrid
10	128.0191	111.6019	94.2282	HO-CPO Hybrid
11	111.4719	103.8349	94.8117	HO-CPO Hybrid
12	125.4802	103.3150	95.0775	HO-CPO Hybrid
13	134.2879	127.1504	112.8849	HO-CPO Hybrid
14	99.6967	97.3642	89.9587	HO-CPO Hybrid
15	102.0299	104.3002	92.2682	HO-CPO Hybrid
16	111.4991	100.7658	83.3481	HO-CPO Hybrid
17	115.8479	95.0608	80.9094	HO-CPO Hybrid
18	132.9363	95.6081	90.7311	HO-CPO Hybrid
19	109.2012	105.2404	77.5431	HO-CPO Hybrid
20	119.1785	106.9864	92.4761	HO-CPO Hybrid

Table 12 reports the omnibus statistics for the same 20 blocks. The Friedman statistic is 36.4000 ($p = 1.2469 \times 10^{-8}$), and the Iman–Davenport transformation gives F = 192.1111 ($p = 1.3509 \times 10^{-20}$). Both tests reject equal rank distributions among the configured procedures.

Table 13 shows the rank structure behind the omnibus rejection. Hybrid HO-CPO has a mean rank of 1.0000, CPO 2.1000, and HO 2.9000, corresponding to rank sums of 20, 42, and 58 across the 20 matched blocks.

Table 14 gives the Holm-adjusted Wilcoxon comparisons. All three pairwise contrasts are significant at the adopted level, and the signed-rank direction favors Hybrid HO-CPO over both standalone procedures and CPO over HO. These differences characterize the configured procedures under unequal evaluation effort.

Table 12. Friedman and Iman–Davenport omnibus test results.

Statistic	Value
Number of runs	20
Number of algorithms	3
Friedman χ^2	36.4000
Df	2
p-value	1.2469×10^{-8}
Iman–Davenport F	192.1111
df1	2
df2	38
p-value	1.3509×10^{-20}
Friedman decision	Reject H_0
Iman–Davenport decision	Reject H_0

Table 13. Mean ranks from the Friedman test.

Algorithm	Average Rank	Rank Sum
HO-CPO Hybrid	1.0000	20
CPO	2.1000	42
HO	2.9000	58

Table 14. Holm-corrected Wilcoxon pairwise comparisons.

Contrast	Raw p-Value	Holm-Adjusted p-Value	Holm Decision	W	z-Value	Lower-Cost Procedure
HO vs. HO-CPO Hybrid	9.5692×10^{-5}	2.8708×10^{-4}	Significant	0	−3.9013	HO-CPO Hybrid
CPO vs. HO-CPO Hybrid	9.5692×10^{-5}	2.8708×10^{-4}	Significant	0	−3.9013	HO-CPO Hybrid
HO vs. CPO	2.7271×10^{-4}	2.8708×10^{-4}	Significant	7	−3.6399	CPO

Table 15 summarizes the same experiment descriptively. The hybrid has the lowest mean cost (88.5465), lowest median (90.3055), a mean rank of 1.0000, and 20 wins in 20 trials. CPO has the smallest standard deviation, so the hybrid's advantage in this experiment is primarily a lower central cost and complete win frequency rather than the narrowest spread.

Table 15. Descriptive statistics and success ranks for the configured procedures.

Rank	Algorithm	Mean Cost	Standard Deviation	Median Cost	Average Rank	Win Count	Win Rate (%)
1	HO-CPO Hybrid	88.5465	9.9220	90.3055	1.0000	20	100
2	CPO	106.0611	9.1208	104.0676	2.1000	0	0
3	HO	119.8542	10.3119	119.4822	2.9000	0	0

Tables 11–15 consistently favor the intensified hybrid under the evaluation effort of the initial experiment. Section 3.2 tests the procedures again with identical evaluation budgets and matched initialization.

3.2. Stage I Equal-Budget Optimizer Comparison

3.2.1. Illustrative Stage I Responses

Table 16 reports the separately seeded illustrative Stage I run at 5050 objective evaluations per procedure. CPO obtains the lowest cost (100.1434), followed by Hybrid HO-CPO

(104.2164) and HO (120.3435). CPO also has the smallest ITAE, RMSE, plateau error, and mean settling time. The hybrid's peak current is 34.9859 A, below the 35 A threshold. Figure 10 shows the corresponding trajectories. This illustrative run is distinct from the 20-run statistical sample.

Table 16. Illustrative equal-budget performance of HO, CPO, and Hybrid HO-CPO.

Metric	HO	CPO	Hybrid HO-CPO
Cost	120.3435	100.1434	104.2164
ITAE	29.6690	23.7184	24.9949
RMSE (rad/s)	23.4631	22.0247	22.6724
Tail error (rad/s)	0.1790	0.0702	0.3005
Plateau error	0.1410	0.0471	0.1086
Mean rise (s)	0.207	0.178	0.191
Mean settling (s)	0.446	0.350	0.483
OS (%)	8.009	7.704	8.142
Peak current (A)	34.788	35.384	34.986
FEs	5050	5050	5050

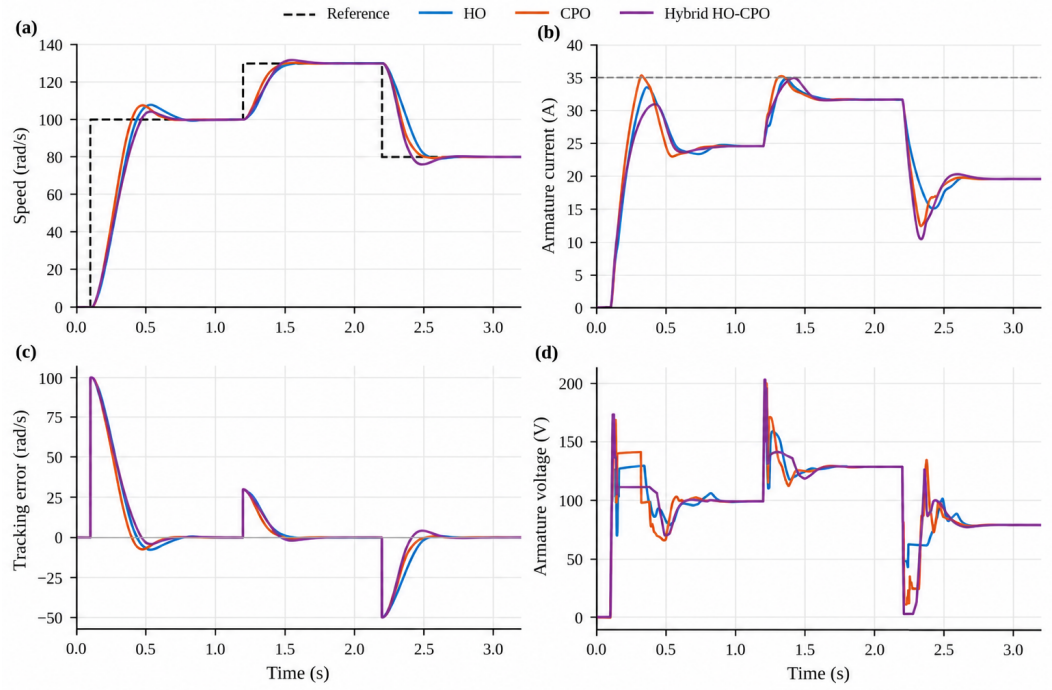


Figure 10. Equal-budget representative responses: (**a**) speed tracking; (**b**) armature current; (**c**) tracking error; (**d**) armature voltage.

Figure 10 presents speed, armature current, tracking error, and voltage for the separately seeded illustrative run. These traces show the tracking and electrical contributions to the scalar cost. Repeated-run behavior is assessed separately below.

3.2.2. Stage I Objective-Component Decomposition

Table 17 decomposes the illustrative costs. CPO has smaller weighted ITAE, ISE, tail-error, and plateau-error terms than the hybrid. The hybrid has a smaller overshoot term and no current-threshold penalty, but these differences do not offset its larger tracking terms in this run.

Table 17. Weighted objective components for the representative equal-budget solutions.

Metric	HO	CPO	Hybrid HO-CPO
Weighted ITAE	29.669	23.718	24.995
Weighted ISE	35.244	31.055	32.909
Weighted tail error	1.790	0.702	3.005
Weighted plateau error	1.692	0.566	1.303
Weighted overshoot	30.280	24.527	21.813
Weighted voltage variation	0.060	0.091	0.077
Weighted current violation	0.000	0.786	0.000
Weighted oscillation	21.609	18.699	20.115
Total	120.344	100.143	104.216

3.2.3. Stage I Twenty-Run Statistical Comparison

Across the 20 matched runs (Table 18), the hybrid has the lowest mean cost (107.5093), median (104.9386), and standard deviation (7.6700). It is the lowest-cost procedure in 15 blocks, compared with five for CPO and none for HO. Mean optimization times are similar: 219.29 s for HO, 220.05 s for CPO, and 219.29 s for the hybrid. Each procedure uses the same 5050-evaluation budget.

Table 18. Descriptive statistics for the 20 matched equal-budget optimizer runs.

Algorithm	Mean Cost	Std.	Median	Mean Optimization Time (s)	Mean FEs	Wins/20
HO	131.1904	12.0218	132.9535	219.29	5050	0
CPO	114.8554	13.0821	114.3672	220.05	5050	5
Hybrid HO-CPO	107.5093	7.6700	104.9386	219.29	5050	15

Table 19 reports the statistical tests for the equal-budget study. The Friedman statistic is $\chi^2 = 30.10$ ($p = 2.91 \times 10^{-7}$), and the Iman–Davenport statistic is F = 57.77 ($p = 3.01 \times 10^{-12}$; df1 = 2, df2 = 38). Holm-adjusted Wilcoxon tests remain significant for HO versus CPO (adjusted $p = 5.86 \times 10^{-4}$), HO versus Hybrid HO-CPO (2.66×10^{-4}), and CPO versus Hybrid HO-CPO (0.00642). The pairwise direction favors CPO over HO and Hybrid HO-CPO over both standalone procedures.

Table 19. Equal-budget omnibus and Holm-adjusted pairwise statistical tests.

Test/Comparison	Statistic	Adjusted or Omnibus p	Decision	Lower Median Cost
Friedman omnibus	$\chi^2 = 30.10$	2.910×10^{-7}	Reject H0	—
Iman–Davenport	F = 57.77	3.006×10^{-12}	Reject H0	—
HO vs. CPO	W = 8; z = 3.621	5.863×10^{-4}	Significant	CPO
HO vs. Hybrid HO-CPO	W = 0; z = 3.920	2.657×10^{-4}	Significant	Hybrid HO-CPO
CPO vs. Hybrid HO-CPO	W = 32; z = 2.725	6.425×10^{-3}	Significant	Hybrid HO-CPO

Figure 11 plots convergence against objective evaluations. This common horizontal axis permits comparison at the same evaluation effort independently of the number of outer iterations.

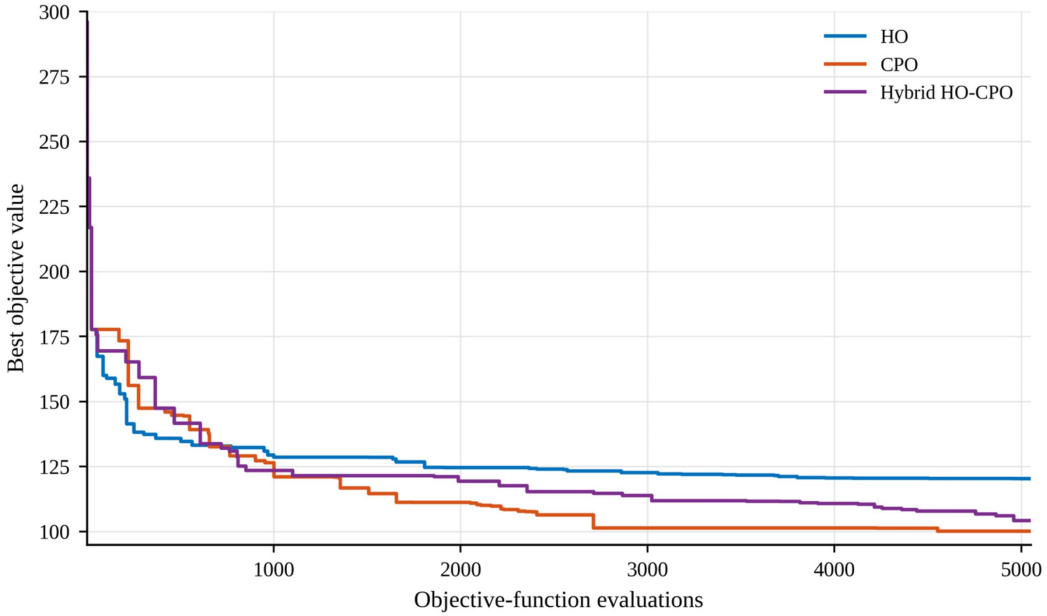


Figure 11. Equal-budget convergence of HO, CPO, and Hybrid HO-CPO plotted against objective-function evaluations.

Figure 12 shows the 20-run cost distributions. The boxplots display the spread around the central values reported in Table 18.

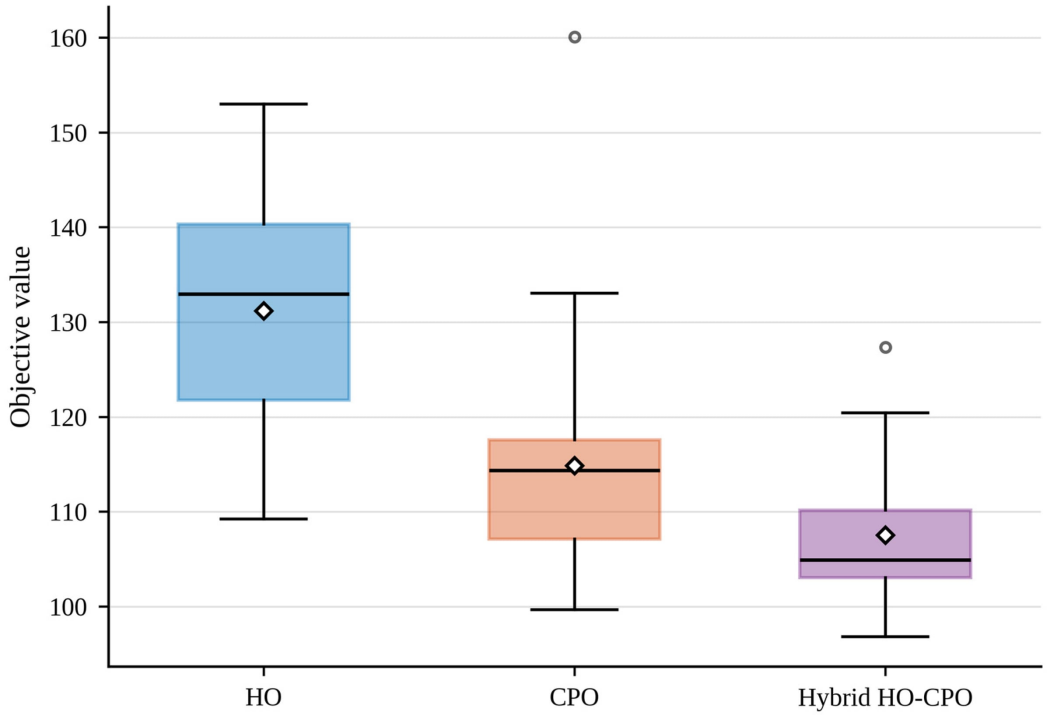


Figure 12. Distribution of objective values over 20 matched equal-budget runs.

Figure 13 presents the mean within-block ranks for the same experiment. These ranks underlie the Friedman and Iman–Davenport comparisons.

The hybrid is selected for Stage II from the 20-run evidence in Tables 18 and 19: it has the lowest mean and median cost and 15 wins. The CPO advantage in the separately seeded illustrative run does not determine the optimizer selection.

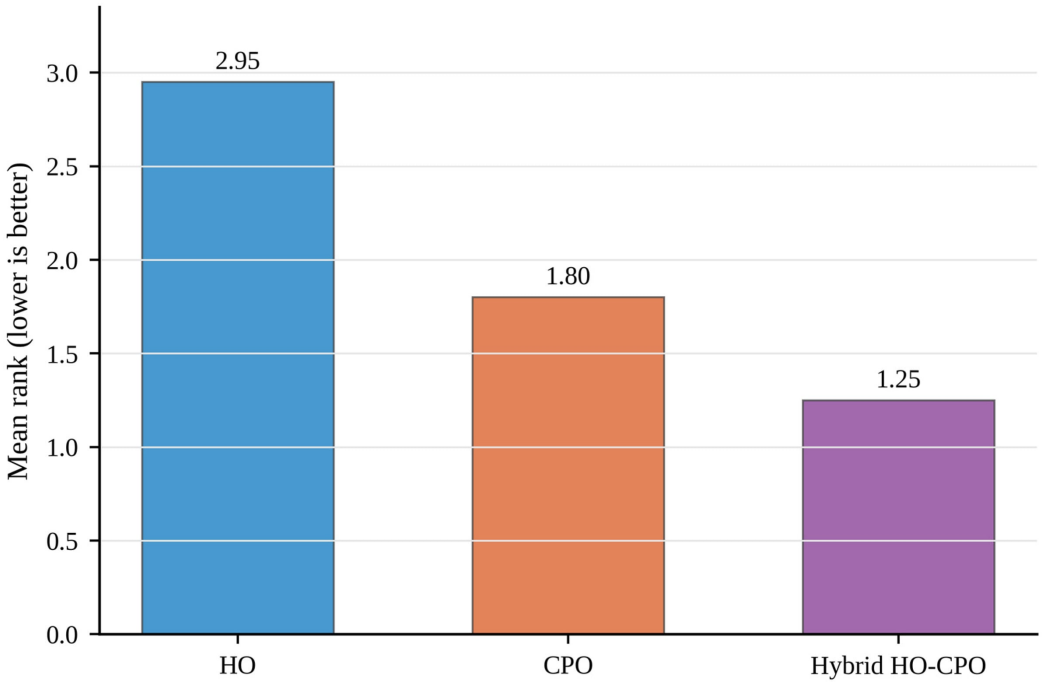


Figure 13. Mean ranks obtained in the equal-budget 20-run comparison.

3.2.4. Stage I Layered Membership Structures Obtained by HO, CPO, and Hybrid HO-CPO

Figures 14–16 show the error, error rate, and consequent partitions obtained for the fixed layered architecture with the three Stage I search procedures. The centers, uncertainty coefficients, and z-levels are those of the selected Stage I controllers. Figures 4–6 refer instead to the initial experiment.

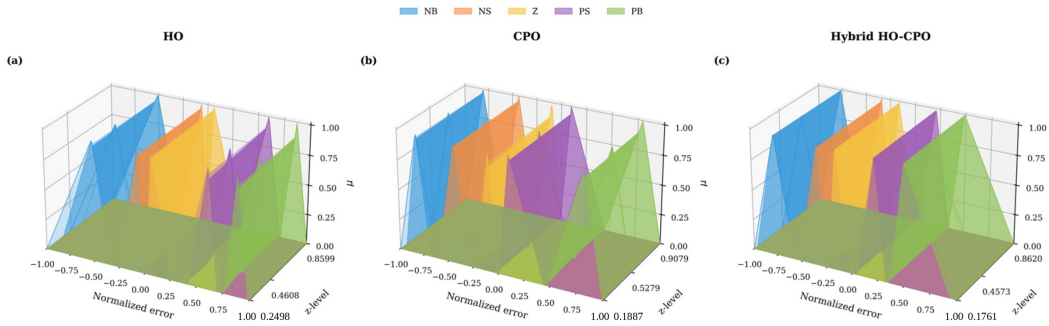


Figure 14. Stage I equal-budget finite T3 error membership structures: (**a**) HO; (**b**) CPO; (**c**) Hybrid HO-CPO.

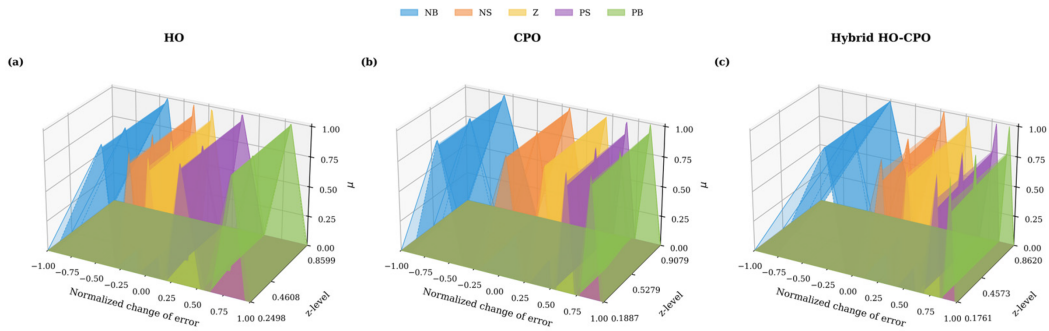


Figure 15. Stage I equal-budget finite T3 change-of-error membership structures: (**a**) HO; (**b**) CPO; (**c**) Hybrid HO-CPO.

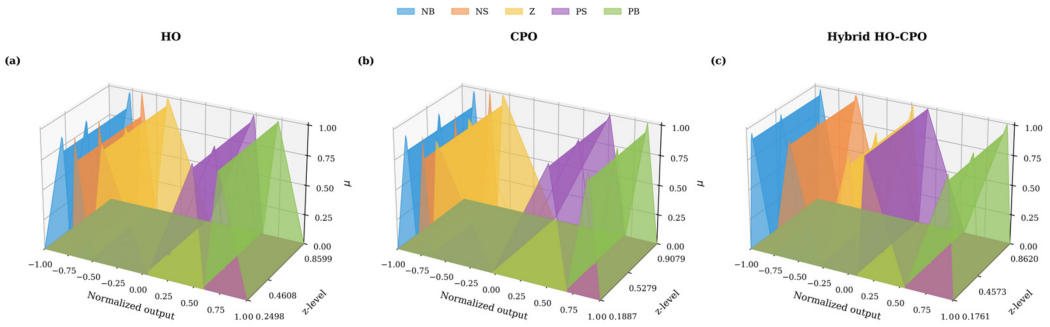


Figure 16. Stage I equal-budget finite T3 output partitions: (**a**) HO; (**b**) CPO; (**c**) Hybrid HO-CPO.

The three procedures produce different antecedent partitions in Figure 14 despite sharing an evaluation budget. HO retains broad central overlap, CPO concentrates several centers in the negative-to-central region, and the hybrid shifts the positive-side sets. The uncertainty widths also differ. These are properties of the selected controllers; the figure alone does not isolate their contribution to performance.

Figure 15 shows the optimized error-rate partitions. Differences in centers and uncertainty widths alter the rule activations as the tracking error increases or decreases. Their effect is assessed through the complete closed-loop responses.

Figure 16 shows the Stage I consequent partitions. Their centers are optimized, but the partition is shared across z-levels because no output-uncertainty vector is present.

3.3. Stage II Controller-Architecture Comparison

Section 3.3 compares independently optimized T1, IT2, and finite T3 designs using the same Hybrid HO-CPO procedure and 5050-evaluation budget. Their gains, memberships, and rule maps may all differ. The comparison therefore evaluates the complete architectures at equal optimization effort.

3.3.1. Aggregate Architecture Results

Table 20 reports mean costs of 106.2192 for T1, 104.6669 for IT2, and 104.6439 for finite T3. The T3–IT2 difference is 0.0230, or approximately 0.022% of the IT2 mean. The 20 paired raw cost rows give Friedman $\chi^2(2) = 0.7000$, $p = 0.7047$, and Iman–Davenport $F(2,38) = 0.3384$, $p = 0.7150$. Thus, the null is not rejected at 0.05, and confirmatory pairwise superiority claims are not supported. This lack of significance does not establish equivalence. Mean ranks are 2.10, 2.05, and 1.85, and mean RMSE values are 22.5571, 22.4224, and 22.2251 rad/s, respectively.

Table 20. Matched T1, IT2, and finite T3 benchmarks using the same Hybrid HO-CPO budget.

Metric	T1	IT2	Finite T3
Mean cost	106.2192	104.6669	104.6439
Std.	7.9046	5.1837	6.7233
Median	105.1478	104.1666	103.6032
Mean ITAE	25.9273	25.4072	25.5712
Mean RMSE (rad/s)	22.5571	22.4224	22.2251
Mean tail error (rad/s)	0.1039	0.1141	0.1429
Mean rise (s)	0.199	0.195	0.194
Mean settling (s)	0.403	0.412	0.414
OS (%)	4.950	6.046	5.259
Peak current (A)	34.589	34.919	34.731
Mean optimization time (s)	49.1	79.3	215.3

For the archived nominal step metrics, rise time is the 10–90% transition interval and overshoot is measured in the direction of the signed reference step. Settling uses a 2% band with a 0.5 rad/s absolute floor. Reported mean rise and settling times average the three reference transitions; maximum overshoot is the largest transition value. The per-transition records are included in the results workbook.

3.3.2. Stage II Representative Closed-Loop Behavior

Table 21 reports the run nearest the median cost within each architecture: run 5 for T1, run 10 for IT2, and run 13 for finite T3. The selected T3 has cost 103.5607, mean settling time 0.366 s, maximum overshoot 0.3765%, peak current 33.2804 A, and terminal mean absolute error 0.00879 rad/s. IT2 has the smallest representative ITAE (25.2973) compared with 25.6650 for T3 and 26.2664 for T1. These selected trajectories are descriptive examples, not paired run-level evidence of structural superiority.

Table 21. Representative T1, IT2, and finite T3 controller performance.

Metric	T1	IT2	Finite T3
Cost	105.7292	104.1198	103.5607
ITAE	26.2664	25.2973	25.6650
RMSE (rad/s)	22.4773	22.2455	22.6339
Tail error (rad/s)	0.06918	0.17129	0.00879
Mean rise (s)	0.189	0.186	0.212
Mean settling (s)	0.418	0.408	0.366
OS (%)	6.019	8.496	0.377
Peak current (A)	34.781	35.098	33.280
Selected run	5	10	13

Figure 17 shows the responses selected nearest to the median cost for each architecture. Their differences reflect both the controller structure and its optimized parameters.

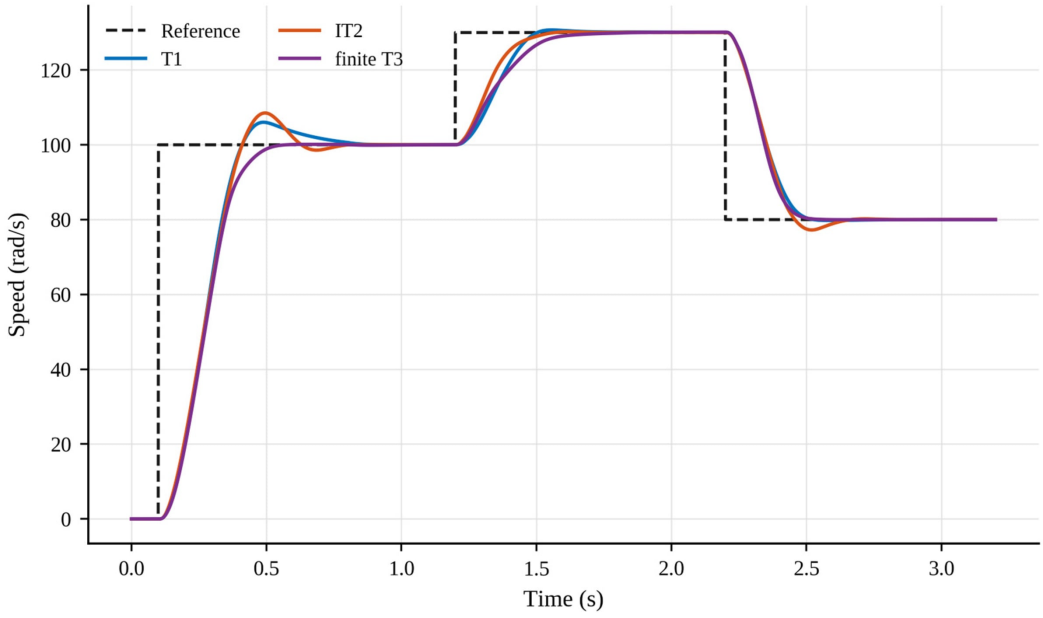


Figure 17. Stage II representative speed responses of T1, IT2, and finite T3 controllers, each optimized with the same Hybrid HO-CPO budget.

Figure 18 shows the corresponding armature currents. Together with the speed traces, these curves describe the electrical demand of each selected response.

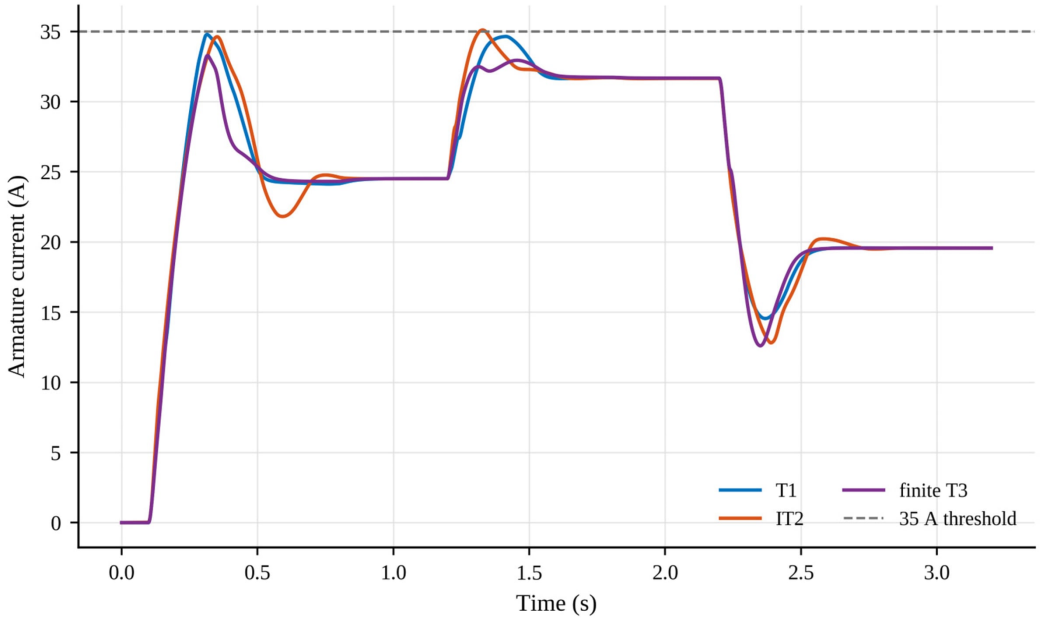


Figure 18. Stage II representative armature-current responses of T1, IT2, and finite T3 controllers, each optimized with the same Hybrid HO-CPO budget.

Table 22 gives the selected gains and layer parameters; Table 23 gives the membership centers and active uncertainty coefficients. Dashes denote inactive quantities. The following figures show each architecture's memberships and rule surface.

Table 22. Optimized global parameters of the representative T1, IT2, and finite T3 controllers obtained with Hybrid HO-CPO.

Parameter	T1	IT2	Finite T3
G_e	0.02557	0.04836	0.02236
G_{de}	0.00432	0.00227	0.00480
G_u	64.15946	65.39727	68.04862
K_i	2.78186	1.28431	1.86856
η	—	0.59738	0.39972
z_1	—	—	0.30274
z_2	—	—	0.51177
z_3	—	—	0.81905
w_{z1}	—	—	0.60816
w_{z2}	—	—	2.02563
w_{z3}	—	—	1.86111

Table 23. Optimized membership-function parameters of the representative T1, IT2, and finite T3 controllers obtained with Hybrid HO-CPO.

Parameter Group	T1	IT2	Finite T3
Error centers	[−0.72767, −0.02756, 0.16687, 0.66865, 0.80718]	[−0.53058, −0.20499, 0.20958, 0.46664, 0.82185]	[−0.66838, −0.54838, −0.20593, 0.32325, 0.64728]
Error uncertainty	–	[0.20742, 0.43634, 0.37792, 0.46872, 0.12950]	[0.23390, 0.32172, 0.42349, 0.26937, 0.21827]
Error-rate centers	[−0.75313, −0.12625, 0.18163, 0.42932, 0.94111]	[−0.84083, −0.12449, 0.00874, 0.44824, 0.69700]	[−0.84357, −0.17354, 0.31433, 0.52340, 0.81975]

Table 23. *Cont.*

Parameter Group	T1	IT2	Finite T3
Error-rate uncertainty	–	[0.27016, 0.30901, 0.11143, 0.40157, 0.35701]	[0.23270, 0.31440, 0.47435, 0.31481, 0.24399]
Output centers	[−0.94514, −0.67449, −0.51806, 0.41203, 0.74883]	[−0.89915, −0.63665, −0.29758, 0.50505, 0.91447]	[−0.94972, −0.53318, 0.34442, 0.52848, 0.64848]

Note: The IT2 and finite T3 formulations used here do not contain a separately optimized output-uncertainty vector. Accordingly, output uncertainty is not listed as an active parameter; the optimized output centers define the available consequent values.

The membership parameters in Table 23 describe how optimization redistributed the linguistic sets. T1 has structurally zero uncertainty. IT2 and finite T3 optimize uncertainty for the two inputs, while their consequents remain crisp values selected from the optimized output centers.

The three structures use the same linguistic labels (NB, NS, Z, PS, and PB), but their optimized partitions and rule maps are not identical. The following subsections therefore report each architecture on its own.

3.3.3. Optimized Type-1 Fuzzy Structure

The optimized Type-1 controller provides the lower-complexity structural reference. Its error centers are −0.7277, −0.0276, 0.1669, 0.6686, and 0.8072; the change-of-error centers are −0.7531, −0.1263, 0.1816, 0.4293, and 0.9411; and the output centers are −0.9451, −0.6745, −0.5181, 0.4120, and 0.7488. The uneven spacing is a result of optimization rather than a manually imposed symmetric partition.

Figure 19 shows the five optimized Type-1 error memberships. Each set assigns one deterministic grade to an input, with no interval footprint or layer dependence.

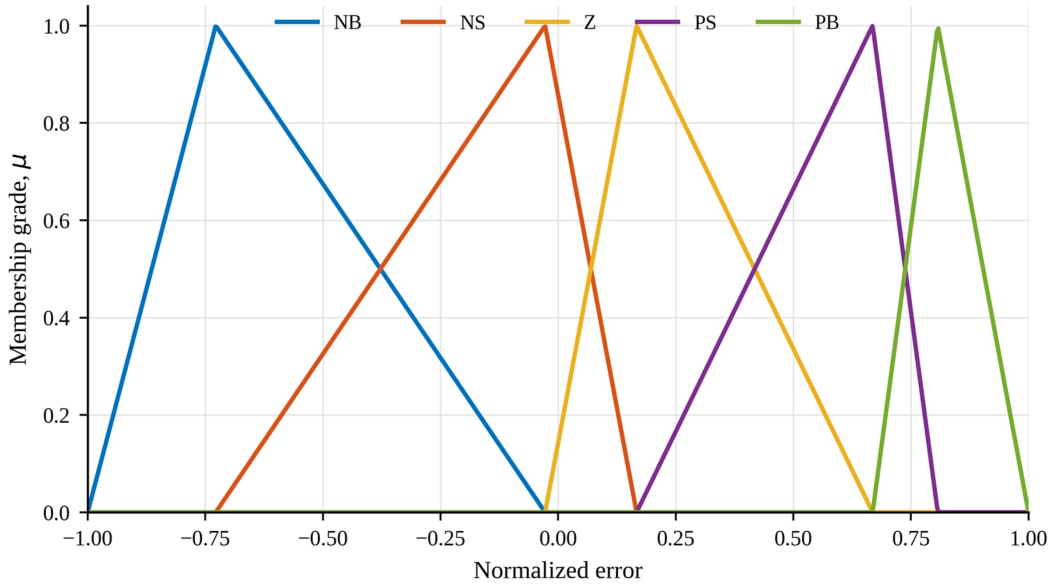


Figure 19. Type-1 error membership functions optimized with Hybrid HO-CPO.

Figure 20 shows the optimized Type-1 error-rate memberships. Their slopes and overlaps determine how changes in tracking error affect rule activation.

Figure 21 shows the Type-1 consequent partition. Its five optimized centers provide the control levels selected by the rule base.

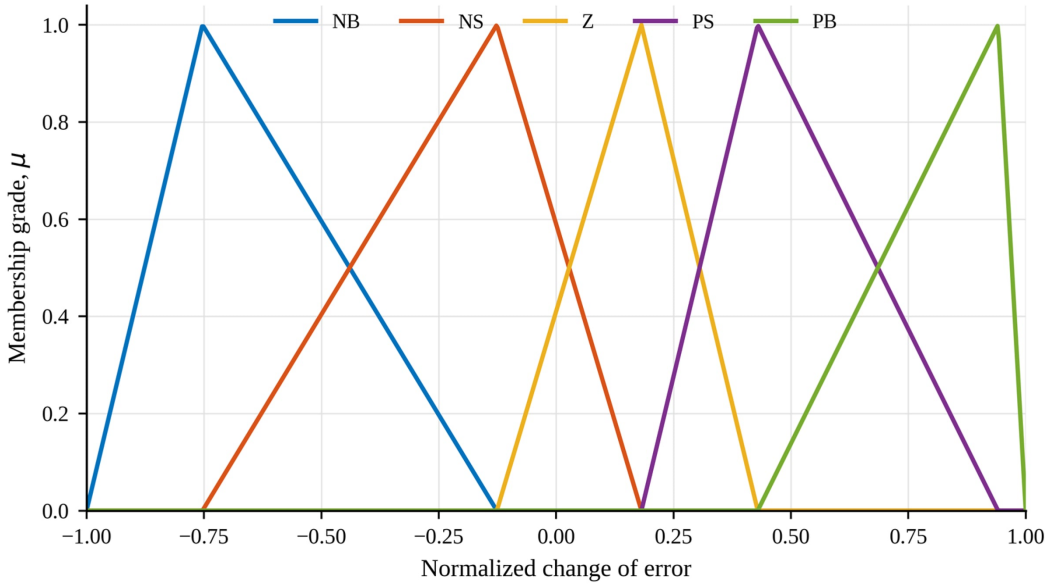


Figure 20. Type-1 error-rate membership functions optimized with Hybrid HO-CPO.

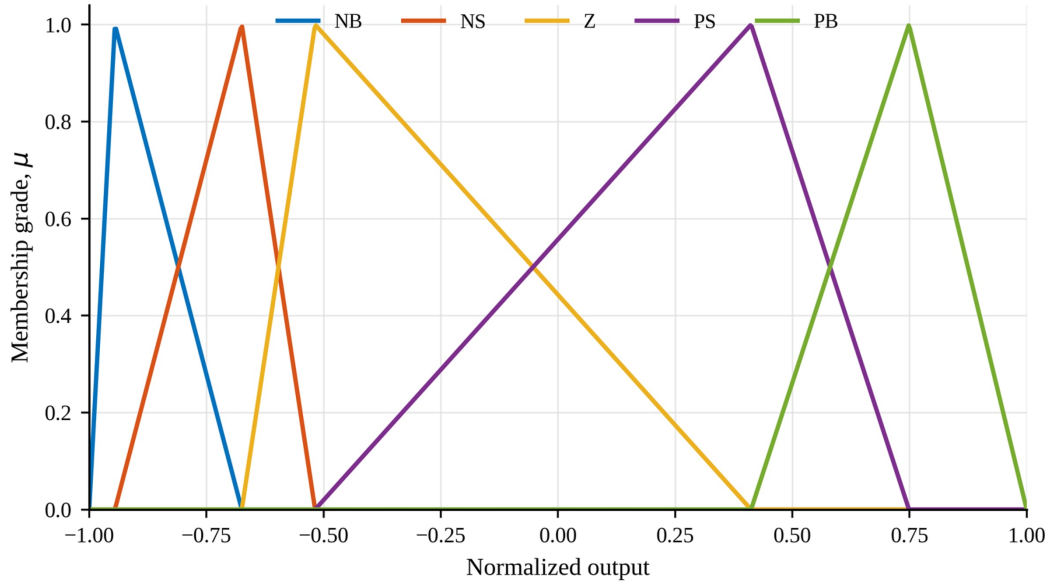


Figure 21. Type-1 consequent partition defined by the optimized output centers.

Table 24 lists the optimized Type-1 rule base. Its non-monotonic entries differ from a conventional diagonal rule map.

Table 24. Optimized 5 × 5 rule base of the representative Type-1 controller.

E/dE	NB	NS	Z	PS	PB
NB	NB	NS	NB	Z	NS
NS	NS	NS	PS	PB	PS
Z	Z	PB	PS	PS	Z
PS	PS	PS	NS	PS	PS
PB	PB	Z	PS	PS	PB

Figure 22 shows the Type-1 input–output surface generated by the optimized memberships and rule base. It makes the local slopes and plateaus of the fuzzy map visible.

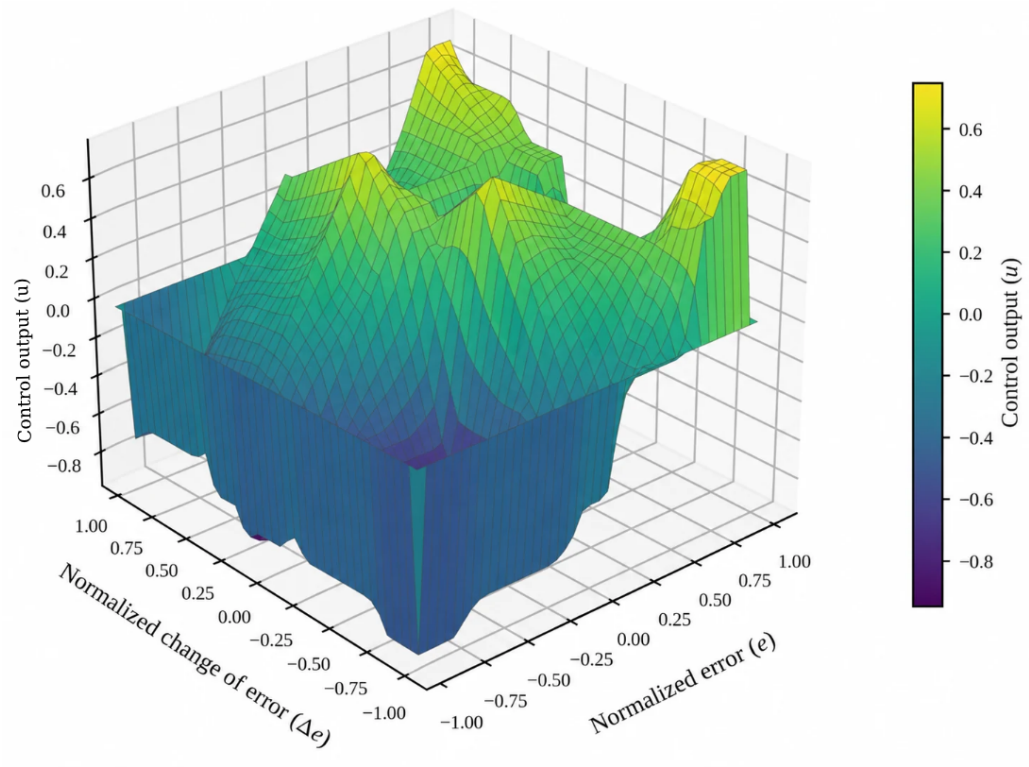


Figure 22. Three-dimensional control surface of the representative Type-1 controller optimized with Hybrid HO-CPO.

3.3.4. Optimized Interval Type-2 Fuzzy Structure

The IT2 solution adds input-side footprints of uncertainty while retaining the same five linguistic labels and 25-rule format. The optimized error uncertainty coefficients range from 0.1295 to 0.4687 and the change-of-error coefficients from 0.1114 to 0.4016. The consequents remain crisp, with no independent output-uncertainty coefficient.

Figure 23 shows the IT2 error sets as upper and lower membership pairs, with their footprints of uncertainty shaded between them.

Figure 24 gives the corresponding IT2 error-rate memberships. The optimized interval widths determine the lower and upper firing strengths in this input channel.

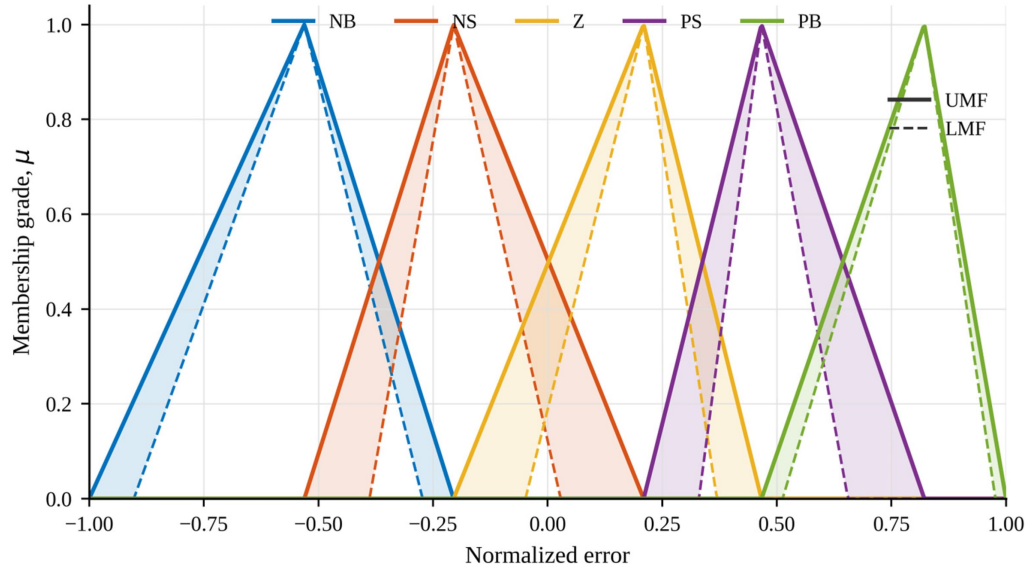


Figure 23. IT2 error memberships and footprints of uncertainty optimized with Hybrid HO-CPO.

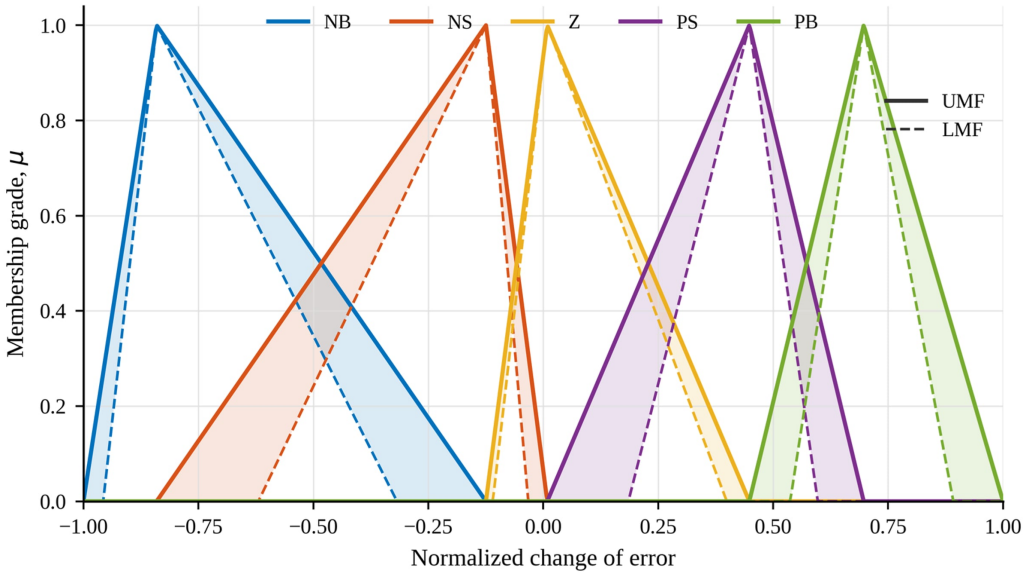


Figure 24. IT2 error-rate memberships and footprints of uncertainty optimized with Hybrid HO-CPO.

Figure 25 shows the shared IT2 consequent partition. The coincident upper and lower curves visualize the optimized center locations. Their areas are not integrated during inference; interval uncertainty enters through the antecedent firing strengths.

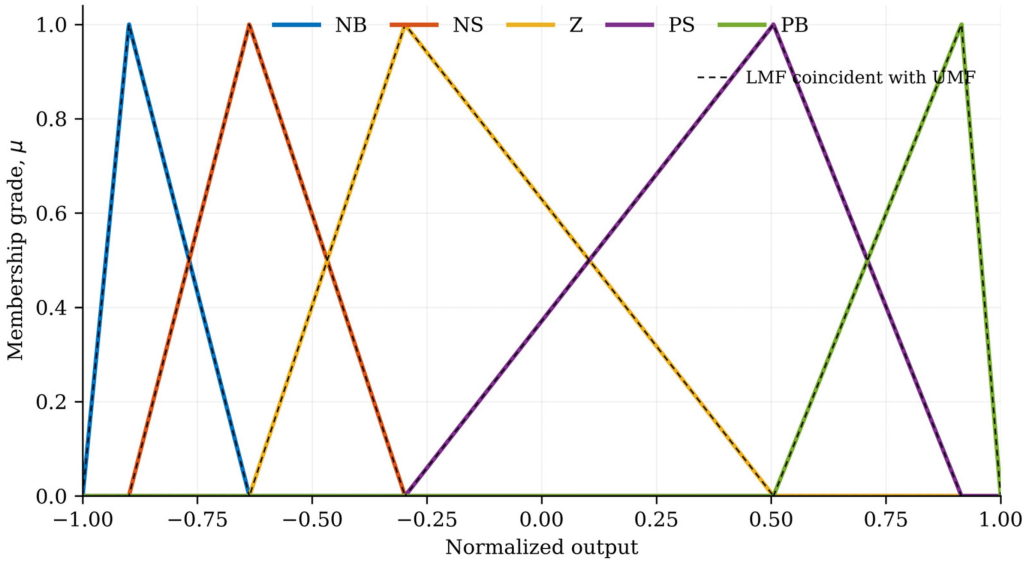


Figure 25. Shared output consequent partition of the representative IT2 controller optimized with Hybrid HO-CPO.

Table 25 lists the optimized IT2 controller rule base.

Table 25. Optimized 5 × 5 rule base of the representative IT2 controller.

E/dE	NB	NS	Z	PS	PB
NB	NB	NB	NB	Z	NS
NS	PS	NS	NB	PB	PS
Z	Z	Z	PB	PS	PB
PS	Z	Z	NS	PS	PS
PB	PS	PS	PB	Z	PB

Figure 26 shows the IT2 control surface obtained from the optimized antecedent footprints, blended firing strengths, and rule map. Both the memberships and consequents differ from those of the Type-1 controller.

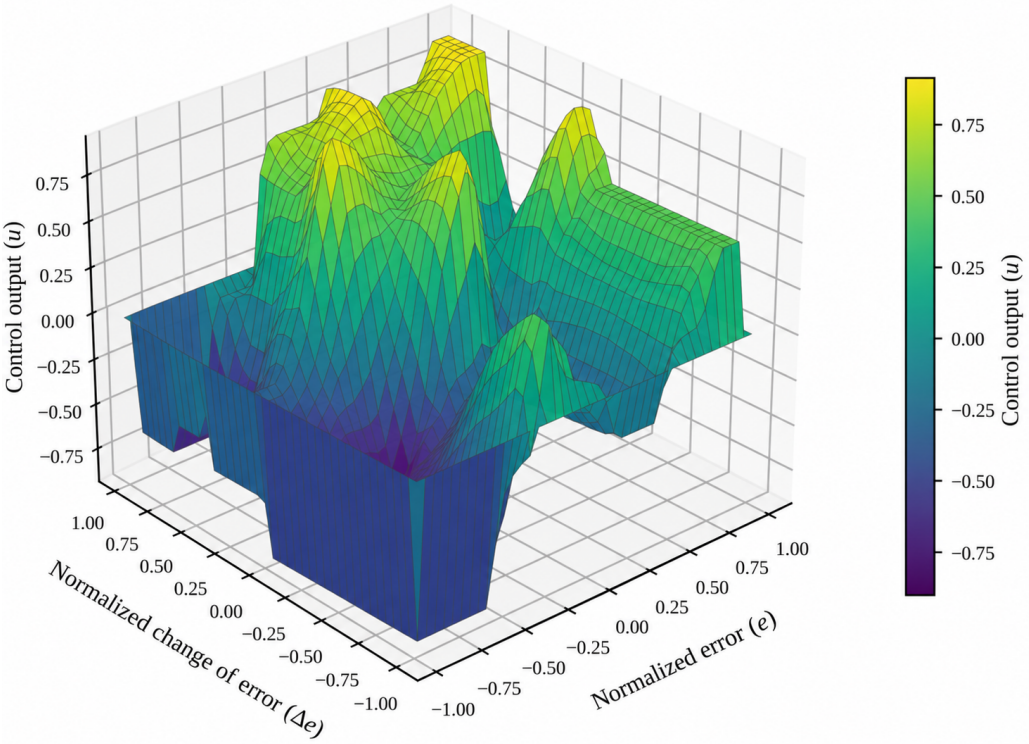


Figure 26. Three-dimensional control surface of the representative IT2 controller optimized with Hybrid HO-CPO.

3.3.5. Optimized Finite z-Slice Layered Fuzzy Structure

The representative finite T3 design uses z-levels of 0.3027, 0.5118, and 0.8191 and positive layer weights of 0.6082, 2.0256, and 1.8611. The input uncertainty coefficients vary among linguistic sets. The output partition is shared across layers.

Figure 27 shows the finite T3 error memberships at the three optimized z-levels. Colors identify the NB–PB sets. The connecting surfaces visualize changes between layers; inference evaluates only the discrete layers.

The change-of-error layered structure uses the same linguistic-set color convention as the other membership plots. Inference uses the three optimized z-levels; the intervening surface is for visualization only. Figure 28 shows the finite T3 error-rate membership structure at the optimized z-levels.

Figure 29 repeats the shared consequent partition at each z-level. The third dimension identifies the layers and does not represent an independently optimized output footprint of uncertainty.

Table 26 gives the optimized finite T3 rule base. Its asymmetric consequent pattern differs from both the T1 and IT2 solutions, showing that the architecture benchmark changed the rule map as well as the uncertainty representation.

Figure 30 shows the finite T3 input-output map formed by separately normalizing each layer output and combining those outputs with the normalized layer weights.

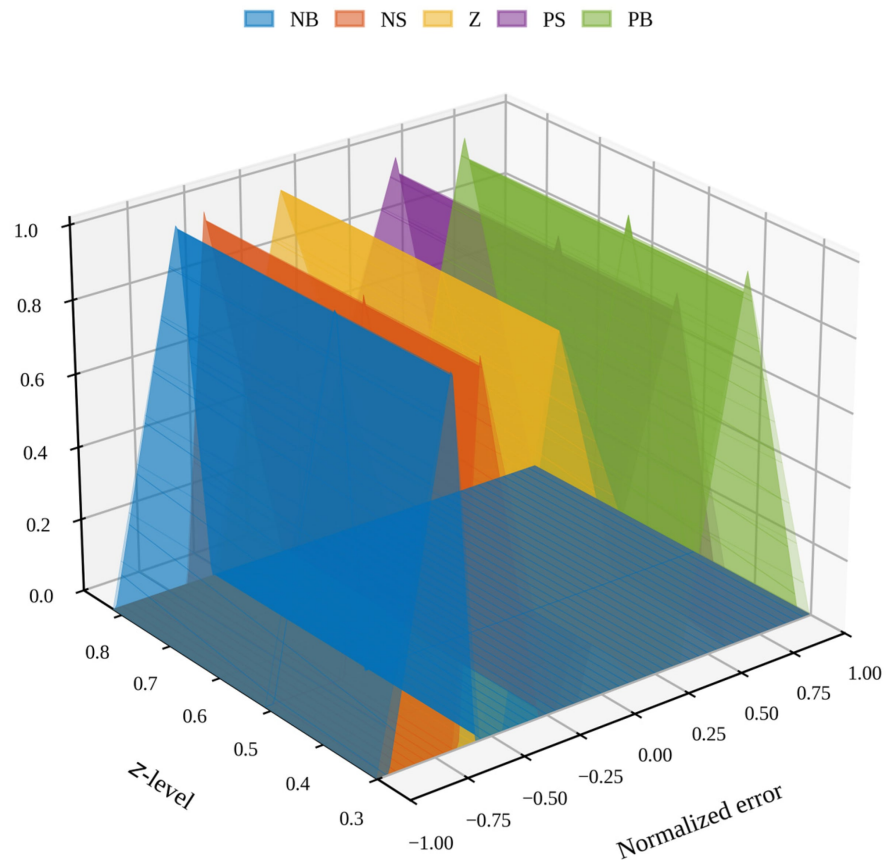


Figure 27. Finite T3 error membership structure at the optimized z-levels.

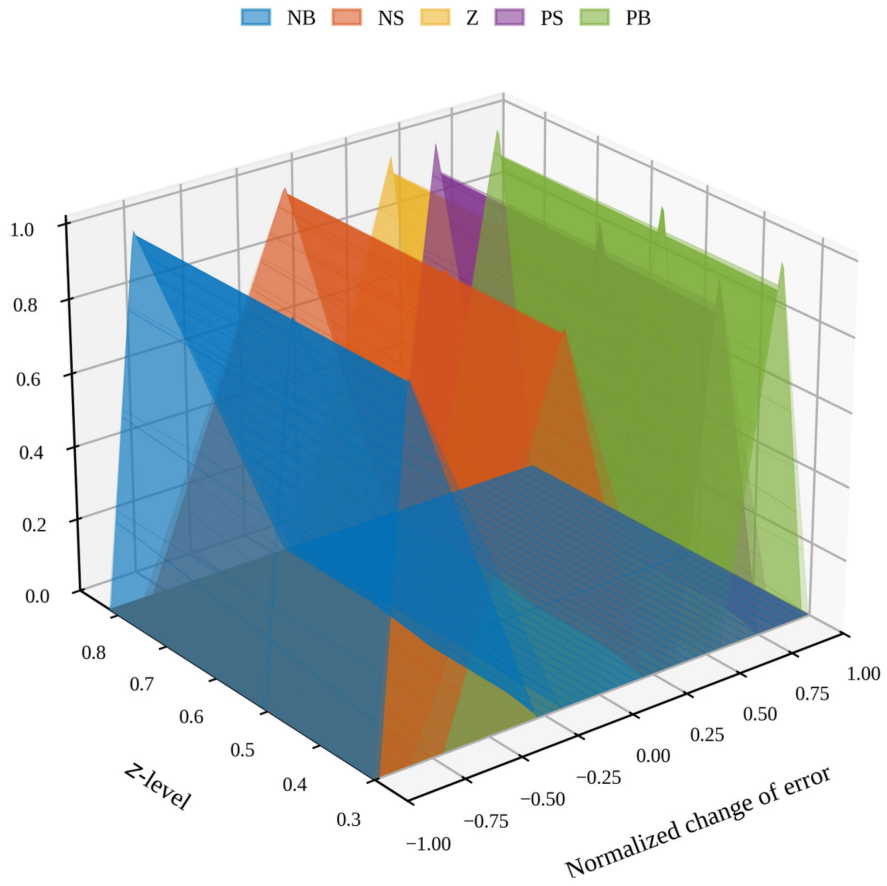


Figure 28. Finite T3 error-rate membership structure at the optimized z-levels.

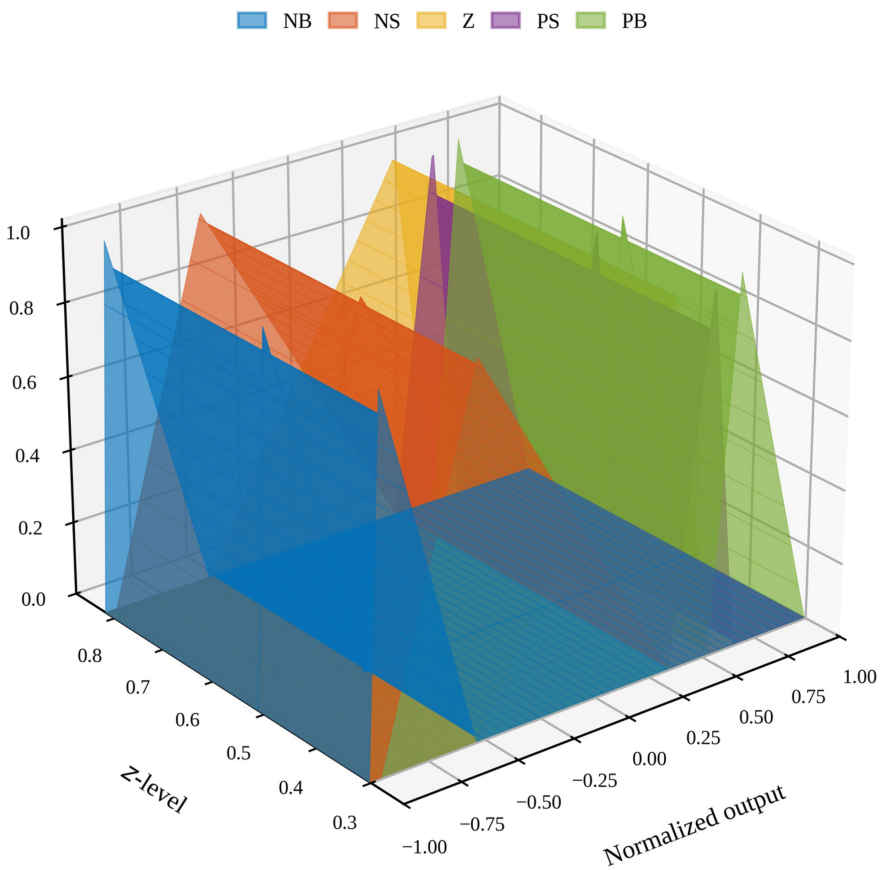


Figure 29. Shared output partition of the representative finite T3 controller optimized with Hybrid HO-CPO; the consequent partition is z-invariant across the optimized z-levels.

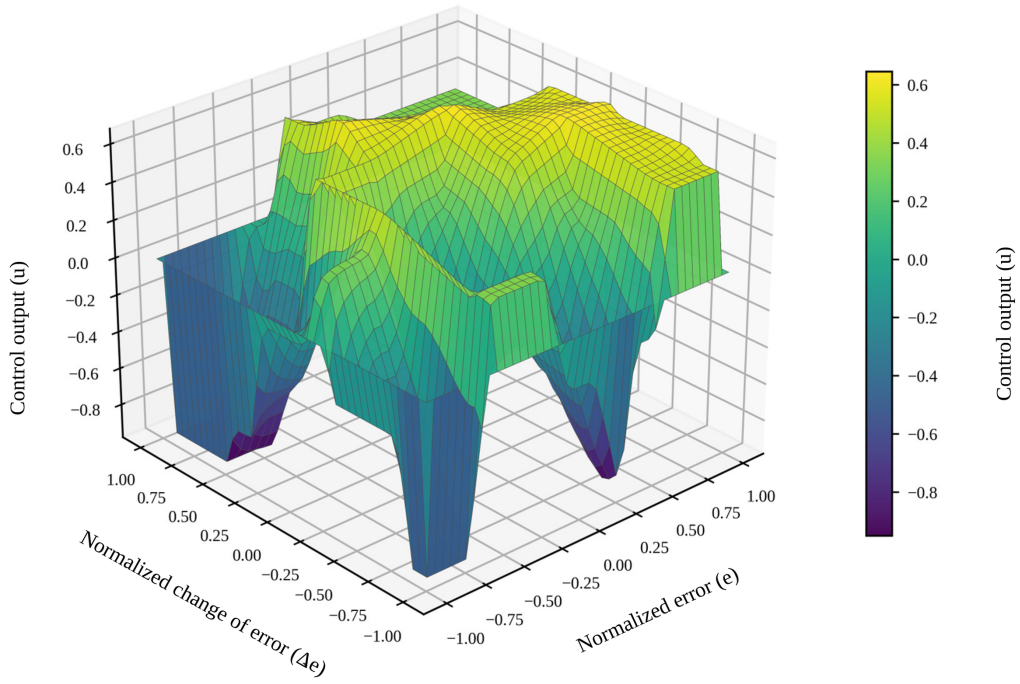


Figure 30. Three-dimensional control surface of the representative finite T3 controller optimized with Hybrid HO-CPO.

Table 26. Optimized 5 × 5 rule base of the representative finite T3 controller.

E/dE	NB	NS	Z	PS	PB
NB	NB	Z	NS	NB	NB
NS	Z	PS	PS	NS	NS
Z	Z	NB	PS	PB	PS
PS	NB	PS	PB	PS	Z
PB	PS	PB	PS	Z	Z

3.4. Robustness Under Parameter, Noise, and Operating-Profile Variations

Under independent ± 20% parameter variation (Table 27), the mean ITAE is 27.3299 for T1, 26.9532 for IT2, and 26.9363 for T3. The corresponding worst values are 32.5983, 47.3418, and 32.2787. T3 also has the smallest mean peak current (34.0931 A) and worst peak current (42.6427 A) in this scenario. These descriptive results use controller-specific random streams and parameter-aware feedforward, as specified in Section 2.5.4.

Table 27. Robustness summary for the representative T1, IT2, and finite T3 controllers.

Scenario and Metric	T1	IT2	Finite T3
Nominal (N = 1)			
Mean ITAE	26.266	25.297	25.665
Worst ITAE	26.266	25.297	25.665
Mean RMSE (rad/s)	22.477	22.245	22.634
Mean tail error (rad/s)	0.069	0.171	0.009
Mean settling (s)	0.418	0.408	0.366
Mean peak current (A)	34.781	35.098	33.280
Worst peak current (A)	34.781	35.098	33.280
Parameter variation ± 20% (N = 50)			
Mean ITAE	27.330	26.953	26.936
Worst ITAE	32.598	47.342	32.279
Mean RMSE (rad/s)	22.704	22.231	22.636
Mean tail error (rad/s)	0.170	0.968	0.426
Mean settling (s)	0.433	0.412	0.437
Mean peak current (A)	36.936	35.915	34.093
Worst peak current (A)	46.945	48.278	42.643
Measurement noise (N = 50)			
Mean ITAE	26.637	25.682	25.990
Worst ITAE	27.116	25.965	26.466
Mean RMSE (rad/s)	22.288	22.063	22.426
Mean tail error (rad/s)	0.257	0.313	0.149
Mean settling (s)	0.433	0.418	0.352
Mean peak current (A)	34.752	35.098	33.282
Worst peak current (A)	34.841	35.223	33.385
Alternative reference and load (N = 1)			
Mean ITAE	50.470	48.678	53.083
Worst ITAE	50.470	48.678	53.083
Mean RMSE (rad/s)	24.760	24.441	24.898
Mean tail error (rad/s)	8.142	7.198	9.582
Mean settling (s)	0.449	0.420	0.465
Mean peak current (A)	38.427	40.538	38.257
Worst peak current (A)	38.427	40.538	38.257
Combined (N = 50)			
Mean ITAE	50.920	54.799	52.410
Worst ITAE	68.773	71.115	62.364
Mean RMSE (rad/s)	24.623	24.829	24.629
Mean tail error (rad/s)	8.255	9.693	9.293
Mean settling (s)	0.473	0.470	0.442
Mean peak current (A)	39.042	41.554	38.925
Worst peak current (A)	53.103	52.535	51.529

Under measurement noise, IT2 has the lowest mean ITAE (25.682), followed by T3 (25.990) and T1 (26.637). In the alternative profile, mean ITAE is 48.678 for IT2, 50.470 for T1, and 53.083 for T3; the corresponding terminal errors are 7.198, 8.142, and 9.582 rad/s. In the combined case, T1 has the lowest mean ITAE (50.920), while T3 has the lowest worst ITAE (62.364). The relatively large alternative-profile terminal errors show that nominal tuning does not guarantee tight tracking at unseen operating conditions.

Figure 31 compares ITAE across the nominal and disturbed scenarios. The preferred architecture changes with the operating condition, consistent with the numerical results in Table 27.

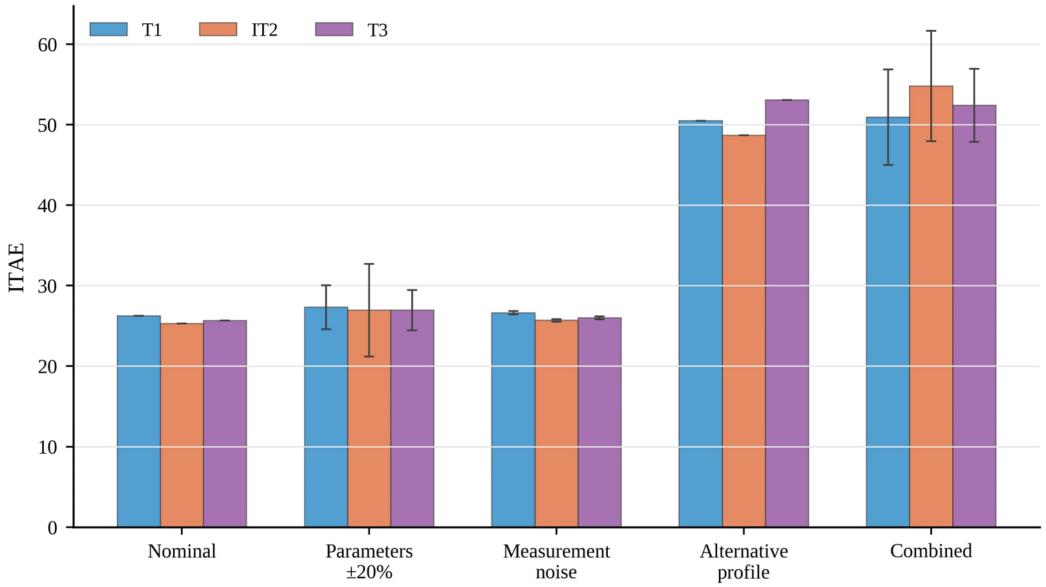


Figure 31. ITAE robustness comparison under nominal, parameter-variation, measurement-noise, alternative-profile, and combined scenarios.

3.5. Current-Protection, Low-Inductance, and Objective-Weight Sensitivity

3.5.1. Soft Penalty Versus Hard-Current Protection

Table 28 compares the nominal soft-penalty simulation with hard-current protection for the selected T3 controller. Both give the same metrics because the peak current is 33.2804 A, below the 35 A threshold. This case therefore tests inactive protection and does not establish performance when the current bound is reached.

Table 28. Soft-current penalty versus hard-current protection for the representative T3 controller.

Metric	Soft Penalty Only	Hard-Current Protection
ITAE	25.6650	25.6650
RMSE (rad/s)	22.6339	22.6339
Tail error (rad/s)	0.00879	0.00879
Mean rise (s)	0.212	0.212
Mean settling (s)	0.366	0.366
OS (%)	0.377	0.377
Peak current (A)	33.280	33.280

Figure 32 confirms that nominal current protection is inactive for the selected T3 controller. An active-limit experiment under a current-demanding disturbance is required to quantify its effect on tracking and recovery.

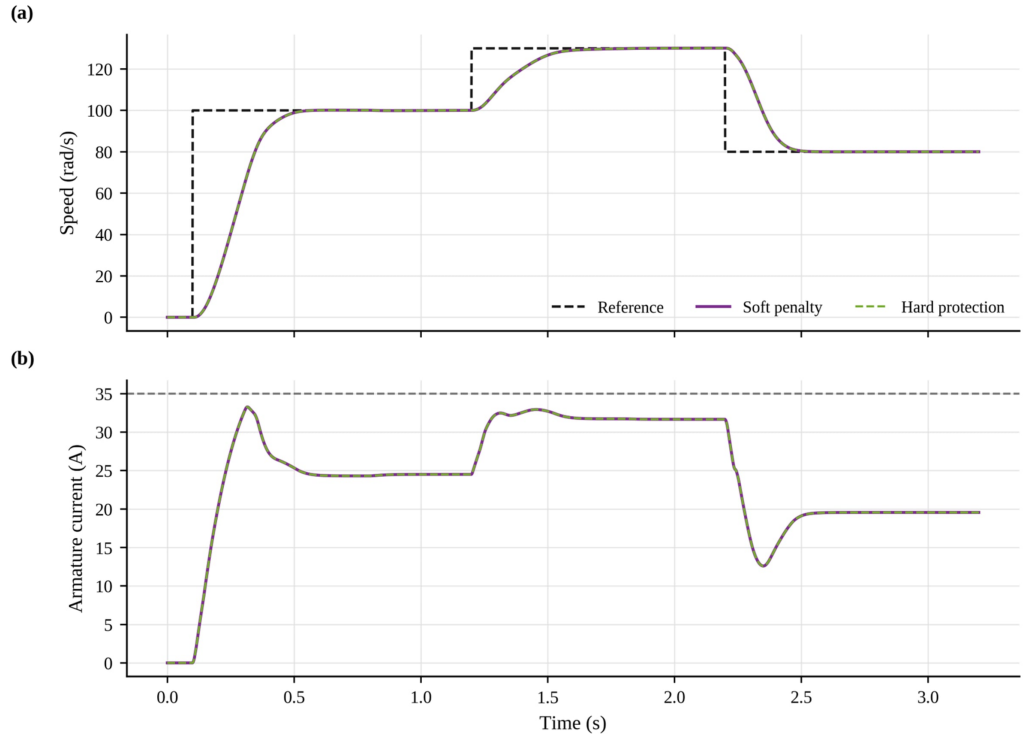


Figure 32. Sensitivity analysis of the representative T3 response under soft penalization and explicit hard-current protection: (**a**) rotor speed response and (**b**) corresponding armature current response.

3.5.2. Low-Inductance Stress Test

Table 29 evaluates the fixed equal-budget T3 controllers as armature inductance is reduced without re-optimization. Lower inductance generally improves tracking speed but increases current demand. At 0.05 H, peak current reaches 50.30 A for HO, 56.77 A for CPO, and 47.85 A for Hybrid HO-CPO. The hybrid has the lowest ITAE at each reduced-inductance point. This is an inductance-sensitivity test of the DC model, not a BLDC approximation, because commutation and inverter switching are not introduced.

Figure 33 shows the tracking and current changes as armature inductance decreases. The controllers remain fixed, so the figure measures their sensitivity to the altered electrical time constant.

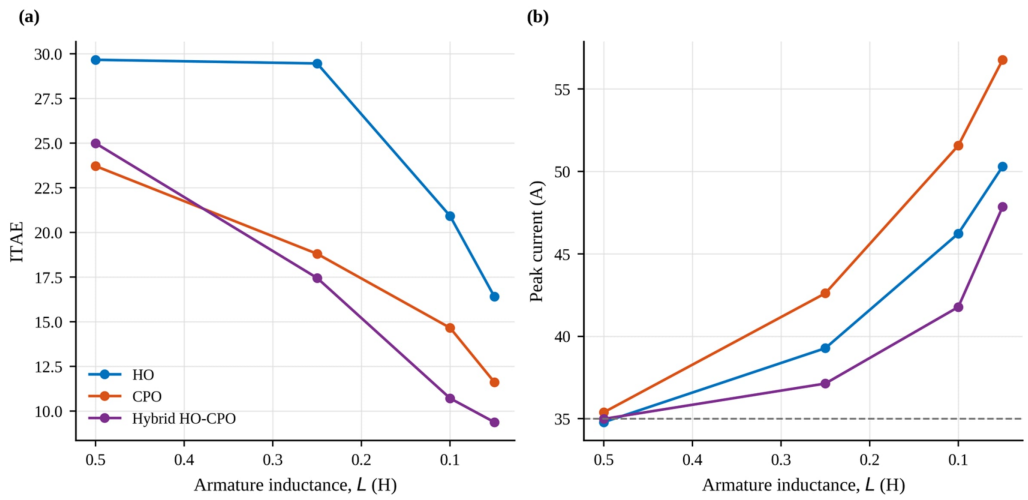


Figure 33. Fixed-controller low-inductance stress test for HO-, CPO-, and Hybrid-HO-CPO-tuned finite T3 controllers: (**a**) ITAE and (**b**) peak current versus armature inductance. The controllers are not re-optimized.

Table 29. Low-inductance stress test using the fixed equal-budget optimized T3 controllers.

Inductance and Metric	HO	CPO	Hybrid HO-CPO
	L = 0.50 H		
ITAE	29.669	23.718	24.995
RMSE (rad/s)	23.463	22.025	22.672
Tail error (rad/s)	0.179	0.070	0.301
Mean settling (s)	0.446	0.350	0.483
OS (%)	8.01	7.70	8.14
Peak current (A)	34.79	35.38	34.99
Peak voltage (V)	159.47	199.75	203.05
	L = 0.25 H		
ITAE	29.465	18.806	17.453
RMSE (rad/s)	20.032	18.706	19.029
Tail error (rad/s)	3.440	0.205	0.079
Mean settling (s)	0.482	0.339	0.330
OS (%)	28.42	15.42	13.96
Peak current (A)	39.28	42.61	37.13
Peak voltage (V)	158.36	199.27	203.03
	L = 0.10 H		
ITAE	20.924	14.661	10.717
RMSE (rad/s)	16.469	15.521	15.558
Tail error (rad/s)	1.351	0.185	0.036
Mean settling (s)	0.367	0.265	0.162
OS (%)	27.00	22.74	5.38
Peak current (A)	46.23	51.57	41.77
Peak voltage (V)	157.47	198.92	203.01
	L = 0.05 H		
ITAE	16.406	11.620	9.381
RMSE (rad/s)	14.568	13.773	13.828
Tail error (rad/s)	0.593	0.130	0.040
Mean settling (s)	0.398	0.243	0.193
OS (%)	19.28	18.12	0.04
Peak current (A)	50.30	56.77	47.85
Peak voltage (V)	157.25	198.78	203.00

3.5.3. Objective-Weight Sensitivity

The objective-weight analysis re-scores the three fixed illustrative Stage I controllers. CPO has the lowest cost under all four named weight sets and all 100 random ± 25% perturbations, followed by the hybrid and HO. This result applies to the selected fixed solutions, whereas the 20-run Stage I experiment compares repeated search outcomes. The unchanged ordering therefore indicates local robustness of these three solutions to the tested weighting changes; it does not imply that the same ranking would necessarily be obtained after complete re-optimization under each alternative weight vector. This distinction is important when sensitivity information is used to interpret an optimized solution [45]. The results of the objective-weight sensitivity analysis are presented in Table 30.

Table 31 summarizes the 100 random perturbations of the eight objective weights. Each perturbed vector re-scores the existing controllers; none of the controllers is retuned for these weights.

Figure 34 shows the costs under the perturbed weights. The ranking of these fixed solutions is unchanged over the tested perturbations.

Figure 35 shows the illustrative Stage I voltage responses. Voltage activity contributes to the objective and is constrained by the command amplitude and nominal per-step increment limits.

Table 30. Named objective-weight sensitivity schemes for the fixed representative equal-budget solutions.

Weight Scheme	Lowest-Cost Procedure	HO Cost	CPO Cost	Hybrid Cost
Nominal	CPO	120.344	100.143	104.216
Tracking-focused	CPO	139.858	115.803	121.150
Electrical-stress-focused	CPO	104.313	87.564	90.552
Oscillation/settling-focused	CPO	122.055	101.709	106.790

Table 31. Summary of 100 random ± 25% objective-weight perturbations.

Algorithm	Mean Cost	Std.	Median	Mean Rank	Wins	Win Rate (%)
HO	120.834	8.639	120.831	3.00	0	0.0
CPO	100.544	7.271	100.368	1.00	100	100.0
Hybrid HO-CPO	104.583	7.450	104.317	2.00	0	0.0

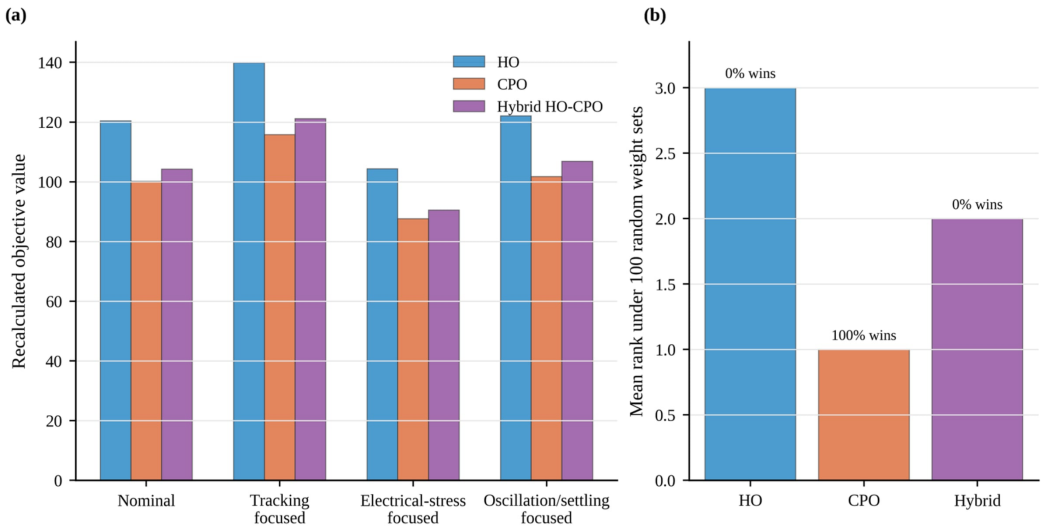


Figure 34. Objective-weight sensitivity of the fixed representative equal-budget controller solutions: (**a**) re-scored objective cost under the four named weight schemes and (**b**) mean rank with win-rate annotation over 100 random ± 25% perturbations. The controllers are not retuned.

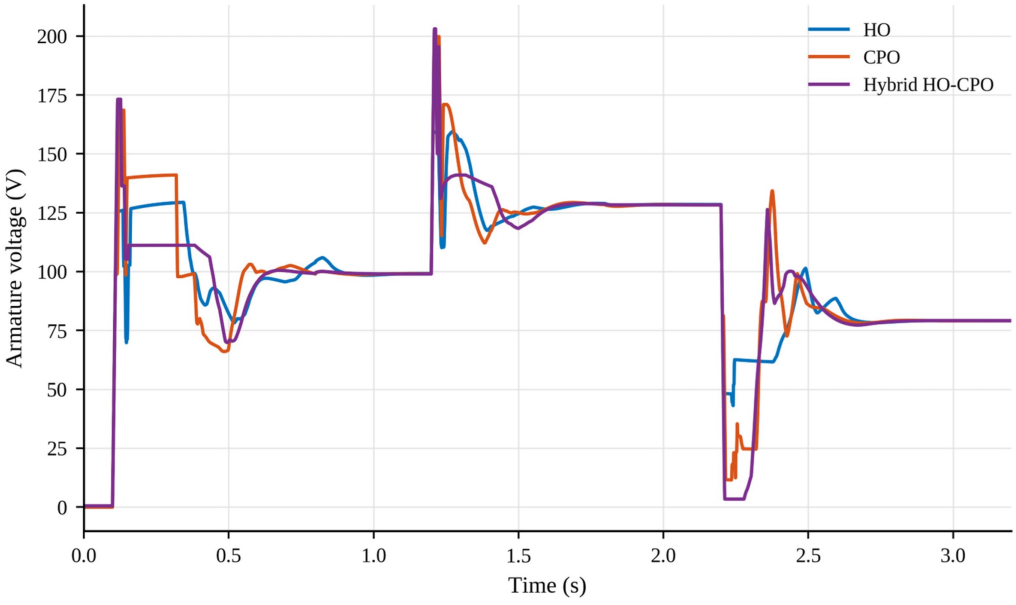


Figure 35. Armature-voltage responses of the representative equal-budget HO, CPO, and Hybrid HO-CPO solutions.

4. Discussion

4.1. Intensified Search and Stage I Optimizer Selection

The initial experiment assesses the complete intensified procedure, whereas Stage I compares search performance at a fixed evaluation budget. The intensified procedure combines preliminary elite information, multiple trial moves, archive use, local refinement, and restarts under unequal evaluation effort. Stage I fixes the layered controller and gives each search procedure 5050 evaluations, allowing the implemented optimizers to be compared at a common budget.

The repeated Stage I experiment favors the hybrid. It has the lowest mean and median cost, the smallest standard deviation, and 15 wins in 20 matched runs. Friedman, Iman–Davenport, and Holm-adjusted Wilcoxon tests identify significant differences. CPO gives a better separately seeded illustrative solution, but optimizer selection for Stage II uses the full repeated-run results.

4.2. Stage II Architecture Comparison

Stage II does not establish a cost advantage for one architecture: Friedman $p = 0.7047$ and Iman–Davenport $p = 0.7150$. The mean T3 cost is only about 0.022% below IT2. The selected T3 has low overshoot and peak current, but these descriptive features do not establish structural superiority. Each architecture also retunes its gains, memberships, and rules, so the comparison cannot isolate uncertainty order as the sole cause of a response difference.

4.3. Complexity, Robustness, and Electrical Stress

The mean recorded optimization time is 49.10 s for T1, 79.32 s for IT2, and 215.33 s for finite T3 at the same 5050-evaluation budget. T3 therefore takes about 4.39 times the T1 time and 2.71 times the IT2 time in these runs. These are total offline search times, including repeated simulations and optimizer overhead. They do not measure per-sample inference latency, memory use, or compliance with a 1 ms embedded deadline.

The preferred controller changes across robustness scenarios. IT2 has lower mean ITAE under measurement noise and in the alternative profile, while T1 has the lowest mean ITAE in the combined scenario. T3 performs well on several peak-current and worst-case measures. Parameter variation also changes the feedforward calculation, so the experiment does not establish rejection of an unknown plant mismatch under fixed nominal feedforward. Reduced inductance improves tracking in the reported tests but substantially increases the transient current.

4.4. Quantitative Positioning Against Related Motor-Control Studies

Table 32 places the results alongside selected fuzzy and metaheuristic motor-control studies [21,22,29,37,41]. It retains each study's plant, command, and validation conditions. The numerical values provide context across adaptive DC control, coordinated armature/field control, BLDC tuning, embedded IT2 control, and Type-3 induction-motor control; they do not form a common benchmark.

Recent studies place the present results in a wider electric-drive and optimization context. Zero-speed sensorless PMSM operation emphasizes observer design and low-speed observability [42], whereas the hybrid RBF-ADALINE framework addresses harmonic estimation and suppression rather than the speed-loop architecture studied here [43]. The negative-salient PMSM study further shows that transient control behavior depends on machine saliency and dq-axis current allocation [44]. These differences prevent direct numerical comparison with the armature-controlled DC model used in this work. The closest methodological connection is the explicit use of sensitivity analysis to qualify how an optimized design depends on parameters and objective assumptions [45].

Table 32. Quantitative context of the present controller against related fuzzy and metaheuristic motor-speed-control studies.

Study	Drive, Controller, and Test Condition	Reported Transient Metrics	Interpretive Context
Ramadan et al. [21]	DC motor; AFLC-PIDAM. FPGA-oriented implementation with a 50–150 rpm square command.	tr = 0.92 s; ts = 2.10 s; overshoot = 3.77 rpm; RMSE = 4.2012 (reported sine-command metric).	Adaptive fuzzy controller with hardware-oriented validation.
Sadiq et al. [22]	Separately excited DC motor; combined armature/field FLC. MATLAB/Simulink at 1000 and 1200 rpm.	ts = 0.121/0.140 s; overshoot = 3.6/0.8%, respectively.	Different actuation strategy and speed range.
Younus et al. [37]	BLDC motor; H-GWO-PI. Simulation under the reported full-load condition.	tr = 0.0344 s; ts = 0.0443 s; overshoot = 0.7031%; RMSE = 0.1827.	Different motor class and a single full-load benchmark.
Chatzipapas and Karnavas [41]	Coreless DC micro-motor; FT2-PID. Experimental STM32/HIL tests over 2000–3500 rpm.	tr = 0.0297–0.0535 s; ts = 0.104–0.167 s; overshoot = 12.0–12.5%.	Hardware validation under embedded processing constraints.
Bal [29]	Induction motor; T3-FLC. Case Study 1, initial −1500 rpm command, 0–3 s interval.	tr = 0.022908 s; ts = 0.043786 s; overshoot = 0.633890%; ess = 0 rpm.	Different motor class; useful direct Type-3 control context.
Present study (initial)	Armature-controlled DC motor; finite T3 + full Hybrid HO-CPO. Simulation with 100-130-80 rad/s multistep reference and scheduled load changes.	mean tr = 0.165 s; mean ts = 0.325 s; max overshoot = 3.967%; RMSE = 21.2247 rad/s; ITAE = 21.7810.	Initial hybrid; unequal evaluation budgets and the initial objective.
Present study (Stage II)	Armature-controlled DC motor; median-near finite T3 design, Hybrid HO-CPO, 5050 evaluations.	mean tr = 0.2123 s; mean ts = 0.3660 s; max overshoot = 0.3765%; RMSE = 22.6339 rad/s; ITAE = 25.6650.	Same architecture budget; no significant cost difference among T1, IT2, and T3.

Note: Values are reproduced as reported in the cited studies. Motor type, reference magnitude, disturbance profile, performance definitions, sampling conditions, and validation platform differ across studies; the table is therefore intended for quantitative context and not for direct ranking.

The cited H-GWO-PI BLDC study reports shorter transient times for its selected full-load condition [37], while the FT2-PID work evaluates settling on embedded hardware [41]. The Type-3 induction-motor study uses a different machine and operating point [29]. Here, the reference is a multistep 100–130–80 rad/s profile with scheduled load changes, and the objective includes current and voltage terms. These differences prevent a direct numerical ranking across studies.

4.5. Limitations and Practical Interpretation

The findings apply to the reduced DC model and the specified inference and search procedures. They do not establish a general Type-3 realization, a Lyapunov stability proof, or equivalence to the canonical optimizers. Robustness scenarios use separate controller-specific random streams and one selected design per architecture. Feedforward is recalculated under parameter variation. The selected nominal T3 remains below the current threshold, leaving active protection untested. Reduced inductance changes the DC dynamics without adding BLDC commutation or inverter switching. Inference latency, memory demand, converter behavior, and hardware performance require further evaluation.

The Supplementary Materials and numerical archive support the Stage I and Stage II cost and statistical calculations. The Supplementary Materials do not specify the exact

MATLAB release or timing hardware, limiting reproducibility of the runtime measurements. They also lack the matching source and time series for the initial experiment and the additional metrics in Table 10.

5. Conclusions

This study jointly tunes controller gains, membership centers, input uncertainty, layer parameters, and 25 rule consequents for DC-motor speed regulation. The finite layered controller is denoted T3 in the experiments. Separate experiments evaluate the initial intensified framework, the implemented optimizers under equal budgets, and independently tuned controller architectures.

At 5050 evaluations per run, the hybrid has the lowest mean cost over 20 matched Stage I runs—107.5093—compared with 114.8554 for CPO and 131.1904 for HO. It wins 15 blocks, and the rank-based comparisons are significant. CPO produces the best separately seeded illustrative solution. The hybrid is selected for Stage II on the basis of the repeated-run evidence.

The Stage II mean costs are 106.2192 for T1, 104.6669 for IT2, and 104.6439 for finite T3, with no significant architecture-level difference across 20 matched blocks. The selected T3 gives 0.3765% overshoot, 0.366 s mean settling time, and 33.2804 A peak current. It is a competitive simulated design, but the small mean-cost difference from IT2 and greater offline optimization time do not support a general claim of higher-order superiority.

Robustness rankings depend on the scenario and metric. T3 has favorable results for several current and worst-case measures, whereas T1 or IT2 can have lower accumulated error. Nominal hard-current protection remains inactive, and reducing inductance increases the transient current. Objective-weight perturbations preserve the ranking of the fixed illustrative Stage I solutions; they do not replace repeated optimization under alternative weights.

Further work should test active current protection, use common disturbance realizations across architectures, and evaluate parameter mismatch with feedforward held at nominal values. Converter-level and hardware-in-the-loop tests should measure inference latency, memory demand, sampling-delay effects, and sensor sensitivity.

Supplementary Materials: The following supporting information can be downloaded at https://zenodo.org/records/23536636 (accessed on 16 October 2026) the Stage I and Stage II results archive, reviewers1_2_revision_outputs, contains MATLAB 2023b workspace and checkpoint files, random seeds, controller vectors, raw costs, robustness and sensitivity results, membership-order checks, an Excel workbook, and PNG/MATLAB FIG plots. The MATLAB source code, dc_motor_reviewers1_2_final_revision_v4.m, is archived on Zenodo (doi.org/10.5281/zenodo.23536636). FULL mode implements the reported protocol; QUICK mode supports preliminary code checks. The supplied implementation covers Stage I and Stage II; the initial intensified-search experiment requires separate source and time-series records.

Funding: This research received no external funding.

Data Availability Statement: The MATLAB source code is publicly available on Zenodo (doi.org/10.5281/zenodo.23536636; record: https://zenodo.org/records/23536636, Access Date: 16 October 2026). The entry point is dc_motor_reviewers1_2_final_revision_v4.m. The numerical outputs for Stage I and Stage II are supplied in reviewers1_2_revision_outputs, including raw costs, controller vectors, random seeds, time-series records, and summary tables. The supplied code covers Stage I and Stage II; reproducing the initial intensified-search experiment requires separate source and time-series records.

Conflicts of Interest: The author declares no conflicts of interest.

References

1. Åström, K.J.; Hägglund, T. The future of PID control. *Control Eng. Pract.* **2001**, *9*, 1163–1175. [CrossRef]
2. Ziegler, J.G.; Nichols, N.B. Optimum settings for automatic controllers. *Trans. Am. Soc. Mech. Eng.* **1942**, *64*, 759–765. [CrossRef]
3. Kennedy, J.; Eberhart, R.C. Particle swarm optimization. In *Proceedings of the ICNN'95—International Conference on Neural Networks (ICNN)*; IEEE: Piscataway, NJ, USA, 1995; Volume 4, pp. 1942–1948. [CrossRef]
4. Volosencu, C. Reducing Energy Consumption and Increasing the Performances of AC Motor Drives Using Fuzzy PI Speed Controllers. *Energies* **2021**, *14*, 2083. [CrossRef]
5. Usama, M.; Kim, J. Improved Self-Sensing Speed Control of IPMSM Drive Based on Cascaded Nonlinear Control. *Energies* **2021**, *14*, 2205. [CrossRef]
6. Jang, J.-S.R. ANFIS: Adaptive-network-based fuzzy inference system. *IEEE Trans. Syst. Man. Cybern.* **1993**, *23*, 665–685. [CrossRef]
7. Karnik, N.N.; Mendel, J.M. Operations on type-2 fuzzy sets. *Fuzzy Sets Syst.* **2001**, *122*, 327–348. [CrossRef]
8. Karnik, N.N.; Mendel, J.M.; Liang, Q. Type-2 fuzzy logic systems. *IEEE Trans. Fuzzy Syst.* **1999**, *7*, 643–658. [CrossRef]
9. Liang, Q.; Mendel, J.M. Interval type-2 fuzzy logic systems: Theory and design. *IEEE Trans. Fuzzy Syst.* **2000**, *8*, 535–550. [CrossRef]
10. Mamdani, E.H.; Assilian, S. An experiment in linguistic synthesis with a fuzzy logic controller. *Int. J. Man.-Mach. Stud.* **1975**, *7*, 1–13. [CrossRef]
11. Mendel, J.M.; John, R.I. Type-2 fuzzy sets made simple. *IEEE Trans. Fuzzy Syst.* **2002**, *10*, 117–127. [CrossRef]
12. Sugeno, M. An introductory survey of fuzzy control. *Inf. Sci.* **1985**, *36*, 59–83. [CrossRef]
13. Takagi, T.; Sugeno, M. Fuzzy identification of systems and its applications to modeling and control. *IEEE Trans. Syst. Man. Cybern.* **1985**, *SMC-15*, 116–132. [CrossRef]
14. Zadeh, L.A. Fuzzy sets. *Inf. Control* **1965**, *8*, 338–353. [CrossRef]
15. Allaoua, B.; Laoufi, A.; Gasbaoui, B.; Abderrahmani, A. Neuro-fuzzy DC motor speed control using particle swarm optimization. *Leonardo Electron. J. Pract. Technol.* **2009**, *15*, 1–18.
16. Garrido, R.; Calderon, D.; Soria, A. Adaptive fuzzy control of DC motors. In *Proceedings of the 10th IEEE International Power Electronics Congress (CIEP)*; IEEE: Piscataway, NJ, USA, 2006; pp. 1–6. [CrossRef]
17. Rahmani, R.; Mahmodian, M.S.; Mekhilef, S.; Shojaei, A.A. Fuzzy logic controller optimized by particle swarm optimization for DC motor speed control. In *Proceedings of the IEEE Student Conference on Research and Development (SCOReD)*; IEEE: Piscataway, NJ, USA, 2012; pp. 109–113. [CrossRef]
18. Ranjani, M.; Murugesan, P. Optimal fuzzy controller parameters using PSO for speed control of quasi-Z source DC/DC converter fed drive. *Appl. Soft Comput.* **2015**, *27*, 332–356. [CrossRef]
19. Rigatos, G.G. Adaptive fuzzy control of DC motors using state and output feedback. *Electr. Power Syst. Res.* **2009**, *79*, 1579–1592. [CrossRef]
20. Tunyasrirut, S.; Ngamwiwit, J.; Furuya, T. Adaptive fuzzy PI controller for speed of separately excited DC motor. In *Proceedings of the 1999 IEEE International Conference on Systems, Man, and Cybernetics (SMC '99)*; IEEE: Piscataway, NJ, USA, 1999; Volume 6, pp. 196–201. [CrossRef]
21. Ramadan, E.A.; El-Bardini, M.; Fkirin, M.A. Design and FPGA-implementation of an improved adaptive fuzzy logic controller for DC motor speed control. *Ain Shams Eng. J.* **2014**, *5*, 803–816. [CrossRef]
22. Sadiq, A.A.; Bakare, G.A.; Anene, E.C.; Mamman, H.B. A fuzzy-based speed control of DC motor using combined armature voltage and field current. *IFAC Proc. Vol.* **2013**, *46*, 387–392. [CrossRef]
23. Castillo, O.; Melin, P. Approach for type-3 fuzzy control. In *Type-3 Fuzzy Logic in Intelligent Control*; Springer: Berlin/Heidelberg, Germany, 2023; pp. 29–44. [CrossRef]
24. Castillo, O.; Melin, P. Interval type-3 fuzzy parameter adaptation in harmony search optimal controller design. In *Type-3 Fuzzy Logic in Intelligent Control*; Springer: Berlin/Heidelberg, Germany, 2023; pp. 63–79. [CrossRef]
25. Castillo, O.; Melin, P. Type-3 fuzzy differential evolution for optimal fuzzy controller parameterization. In *Type-3 Fuzzy Logic in Intelligent Control*; Springer: Berlin/Heidelberg, Germany, 2023; pp. 45–61. [CrossRef]
26. Castillo, O.; Valdez, F.; Melin, P.; Ding, W. A survey on type-3 fuzzy logic systems and their control applications. *IEEE/CAA J. Autom. Sin.* **2024**, *11*, 1744–1756. [CrossRef]
27. Xu, S.; Zhang, C.; Mohammadzadeh, A. Type-3 fuzzy control of robotic manipulators. *Symmetry* **2023**, *15*, 483. [CrossRef]
28. Aliev, R.; Abiyev, R.; Abizada, S. Type-3 fuzzy neural networks for dynamic system control. *Inf. Sci.* **2025**, *690*, 121454. [CrossRef]
29. Bal, C. Type-3 fuzzy logic-based robust speed control for an indirect vector-controlled induction motor. *Appl. Sci.* **2025**, *15*, 11994. [CrossRef]
30. Castillo, O.; Melin, P. A review on interval type-2 fuzzy logic applications in intelligent control. *Inf. Sci.* **2014**, *279*, 615–631. [CrossRef]

31. Castillo, O.; Amador-Angulo, L.; Castro, J.R.; Garcia-Valdez, M. A comparative study of type-1 fuzzy logic systems, interval type-2 fuzzy logic systems and generalized type-2 fuzzy logic systems in control problems. *Inf. Sci.* **2016**, *354*, 257–274. [CrossRef]
32. Castillo, O.; Aguilar, L.T.; Cazarez-Castro, N.R.; Cardenas-Maciel, S.L. Systematic design of a stable type-2 fuzzy logic controller. *Appl. Soft Comput.* **2008**, *8*, 1274–1279. [CrossRef]
33. Castillo, O.; Melin, P.; Alanis, A.; Montiel, O.; Sepulveda, R. Optimization of interval type-2 fuzzy logic controllers using evolutionary algorithms. *Soft Comput.* **2011**, *15*, 1145–1160. [CrossRef]
34. Kumbasar, T. Robust stability analysis and systematic design of single-input interval type-2 fuzzy logic controllers. *IEEE Trans. Fuzzy Syst.* **2016**, *24*, 675–694. [CrossRef]
35. Kumbasar, T.; Hagras, H. A self-tuning zSlices-based general type-2 fuzzy PI controller. *IEEE Trans. Fuzzy Syst.* **2015**, *23*, 991–1013. [CrossRef]
36. Mittal, K.; Jain, A.; Vaisla, K.S.; Castillo, O.; Kacprzyk, J. A comprehensive review on type 2 fuzzy logic applications: Past, present and future. *Eng. Appl. Artif. Intell.* **2020**, *95*, 103916. [CrossRef]
37. Younus, S.M.Y.; Kutbay, U.; Rahebi, J.; Hardalaç, F. Hybrid Gray Wolf Optimization–Proportional Integral Based Speed Controllers for Brush-Less DC Motor. *Energies* **2023**, *16*, 1640. [CrossRef]
38. Kakouche, K.; Oubelaid, A.; Mezani, S.; Rekioua, D.; Rekioua, T. Different Control Techniques of Permanent Magnet Synchronous Motor with Fuzzy Logic for Electric Vehicles: Analysis, Modelling, and Comparison. *Energies* **2023**, *16*, 3116. [CrossRef]
39. Kroičs, K.; Būmanis, A. BLDC Motor Speed Control with Digital Adaptive PID-Fuzzy Controller and Reduced Harmonic Content. *Energies* **2024**, *17*, 1311. [CrossRef]
40. Qin, H.; Wang, L.; Wang, S.; Ruan, W.; Jiang, F. A Fuzzy Adaptive PID Coordination Control Strategy Based on Particle Swarm Optimization for Auxiliary Power Unit. *Energies* **2024**, *17*, 5311. [CrossRef]
41. Chatzipapas, N.V.; Karnavas, Y.L. Adaptive Microprocessor-Based Interval Type-2 Fuzzy Logic Controller Design for DC Micro-Motor Control Considering Hardware Limitations. *Energies* **2025**, *18*, 5781. [CrossRef]
42. Jin, T.; Sun, W.; Zhang, G.; Wang, G.; Jiang, D.; Li, D.; Xu, D. Zero Speed Sensorless Scheme for PMSM Drives Using Virtual Flux Signal Injection Based Hybrid Active Flux Observer. *IEEE Trans. Ind. Electron.* **2026**, *73*, 6657–6668. [CrossRef]
43. Cheng, X.; Qu, S.; He, J.; Zhang, C.; Yang, H. Harmonic Estimation and Suppression for PMSM Drives via a Hybrid RBF-ADALINE Framework. *IEEE J. Emerg. Sel. Top. Power Electron.* **2026**, *early access*. [CrossRef]
44. Chen, X.; Cui, J.; Feng, Y.; Li, Y.X. Research on dq-axis Current Distribution and Control Strategy of a Novel Negative-Salient PMSM for Vehicle. *COMPEL Int. J. Comput. Math. Electr. Electron. Eng.* **2026**, *45*, 1170–1189. [CrossRef]
45. Wang, D.; Cao, R.; Liu, X.; Zheng, S.; Le, Y. Design of Hybrid Magnetic Bearings Based on Integrated Equivalent Magnetic Network Modeling and Sensitivity Analysis for Optimization. *IEEE/ASME Trans. Mechatron.* **2026**, *early access*. [CrossRef]
46. Ghamari, S.M.; Ghahramani, M.; Habibi, D.; Aziz, A. Design of a Robust Adaptive Cascade Fractional-Order Proportional–Integral–Derivative Controller Enhanced by Reinforcement Learning Algorithm for Speed Regulation of Brushless DC Motor in Electric Vehicles. *Energies* **2025**, *18*, 5056. [CrossRef]
47. Saoudi, A.; Krim, S.; Mimouni, M.F. Enhanced Intelligent Closed Loop Direct Torque and Flux Control of Induction Motor for Standalone Photovoltaic Water Pumping System. *Energies* **2021**, *14*, 8245. [CrossRef]
48. Suwongsa, T.; Areerak, K.; Areerak, K.; Pakdeeto, J. Energy Saving Approach for an Electric Pump Using a Fuzzy Controller. *Energies* **2021**, *14*, 3330. [CrossRef]
49. Nhon, P.N.Q.; Elamvazuthi, I.; Fayek, H.M.; Parasuraman, S.; Ahamed Khan, M.K.A. Intelligent control of rehabilitation robot: Auto tuning PID controller with interval type 2 fuzzy for DC servomotor. *Procedia Comput. Sci.* **2014**, *42*, 183–190. [CrossRef]
50. Wang, T.; Wang, H.; Hu, H.; Lu, X.; Zhao, S. An adaptive fuzzy PID controller for speed control of brushless direct current motor. *SN Appl. Sci.* **2022**, *4*, 71. [CrossRef]
51. Abdel-Basset, M.; Mohamed, R.; Abouhawwash, M. Crested Porcupine Optimizer: A new nature-inspired metaheuristic. *Knowl.-Based Syst.* **2024**, *284*, 111257. [CrossRef]
52. Amiri, M.H.; Mehrabi Hashjin, N.; Montazeri, M.; Mirjalili, S.; Khodadadi, N. Hippopotamus optimization algorithm: A novel nature-inspired optimization algorithm. *Sci. Rep.* **2024**, *14*, 5032. [CrossRef]
53. Castillo, O.; Castro, J.R.; Melin, P. *Interval Type-3 Fuzzy Systems: Theory and Design*; Springer: Berlin/Heidelberg, Germany, 2022. [CrossRef]
54. Mendel, J.M.; Liu, F.; Zhai, D. Alpha-plane representation for type-2 fuzzy sets: Theory and applications. *IEEE Trans. Fuzzy Syst.* **2009**, *17*, 1189–1207. [CrossRef]
55. Wu, D. On the fundamental differences between interval type-2 and type-1 fuzzy logic controllers. *IEEE Trans. Fuzzy Syst.* **2012**, *20*, 832–848. [CrossRef]
56. Mizumoto, M.; Tanaka, K. Some properties of fuzzy sets of type 2. *Inf. Control* **1976**, *31*, 312–340. [CrossRef]

57. Wagner, C.; Hagras, H. zSlices—Towards bridging the gap between interval and general type-2 fuzzy logic. In *Proceedings of the IEEE International Conference on Fuzzy Systems (FUZZ-IEEE)*; IEEE: Piscataway, NJ, USA, 2008; pp. 489–497. [CrossRef]
58. Wagner, C.; Hagras, H. Toward general type-2 fuzzy logic systems based on zSlices. *IEEE Trans. Fuzzy Syst.* **2010**, *18*, 637–660. [CrossRef]
59. Mohammadzadeh, A.; Sabzalian, M.H.; Zhang, W. An interval type-3 fuzzy system and a new online fractional-order learning algorithm: Theory and practice. *IEEE Trans. Fuzzy Syst.* **2020**, *28*, 1940–1950. [CrossRef]
60. Qasem, S.N.; Ahmadian, A.; Mohammadzadeh, A.; Rathinasamy, S.; Pahlevanzadeh, B. A type-3 logic fuzzy system: Optimized by a correntropy based Kalman filter with adaptive fuzzy kernel size. *Inf. Sci.* **2021**, *572*, 424–443. [CrossRef]
61. Alkabaa, A.S.; Taylan, O.; Balubaid, M.; Zhang, C.; Mohammadzadeh, A. A practical type-3 fuzzy control for mobile robots: Predictive and Boltzmann-based learning. *Complex Intell. Syst.* **2023**, *9*, 6509–6522. [CrossRef]
62. Baruch, I.S.; Garrido, R.; Flores, J.M.; Martinez, J.C. An adaptive neural control of a DC motor. In *Proceedings of the IEEE International Symposium on Intelligent Control (ISIC'01)*; IEEE: Piscataway, NJ, USA, 2001; pp. 121–126. [CrossRef]
63. Choi, S.B. Sensorless adaptive speed control of a permanent-magnet DC motor for anti-lock brake systems. *Int. J. Automot. Technol.* **2011**, *12*, 207–212. [CrossRef]
64. Minkova, M.D.; Minkov, D.; Rodgerson, J.L.; Harley, R.G. Adaptive neural speed controller of a DC motor. *Electr. Power Syst. Res.* **1998**, *47*, 123–132. [CrossRef]
65. Shahgholian, G.; Shafaghi, P. State space modeling and eigenvalue analysis of the permanent magnet DC motor drive system. In *Proceedings of the 2nd International Conference on Electronic Computer Technology*; IEEE: Piscataway, NJ, USA, 2010; pp. 63–67. [CrossRef]
66. Yildiz, A.B. Electrical equivalent circuit based modeling and analysis of direct current motors. *Int. J. Electr. Power Energy Syst.* **2012**, *43*, 1043–1047. [CrossRef]
67. Gökçe, C.O.; İpek, M.E.; Dayıoğlu, M.; Ünal, R. Parameter estimation and speed control of real DC motor with low resolution encoder. *Results Control Optim.* **2025**, *19*, 100549. [CrossRef]
68. Horng, J.-H. Neural adaptive tracking control of a DC motor. *Inf. Sci.* **1999**, *118*, 1–13. [CrossRef]
69. Molina-Santana, E.; Iturralde Carrera, L.A.; Álvarez-Alvarado, J.M.; Aviles, M.; Rodríguez-Resendiz, J. Modeling and control of a permanent magnet DC motor: A case study for a bidirectional conveyor belt's application. *Eng* **2025**, *6*, 42. [CrossRef]
70. Prakash, R.; Vasanthi, R. Speed control of DC-DC converter fed DC motor using robust adaptive intelligent controller. *J. Vib. Control* **2015**, *21*, 3107–3120. [CrossRef]
71. Rovithakis, G.A.; Christodoulou, M.A. Direct adaptive regulation using dynamic neural networks: Application to DC motors speed control. *Math. Comput. Simul.* **1996**, *41*, 53–62. [CrossRef]
72. Blum, C.; Puchinger, J.; Raidl, G.R.; Roli, A. Hybrid metaheuristics in combinatorial optimization: A survey. *Appl. Soft Comput.* **2011**, *11*, 4135–4151. [CrossRef]
73. Chen, B.; Chen, Y.; Cao, L.; Chen, C.; Yue, Y. An improved crested porcupine optimization algorithm incorporating butterfly search and triangular walk strategies. *Biomimetics* **2025**, *10*, 766. [CrossRef]
74. Cotta, C.; Mathieson, L.; Moscato, P. Memetic algorithms. In *Handbook of Heuristics*; Martí, R., Pardalos, P.M., Resende, M.G.C., Eds.; Springer: Berlin/Heidelberg, Germany, 2016. [CrossRef]
75. Han, T.; Wang, H.; Li, T.; Liu, Q.; Huang, Y. MHO: A modified hippopotamus optimization algorithm for global optimization and engineering design problems. *Biomimetics* **2025**, *10*, 90. [CrossRef]
76. Mou, K.; Zhang, M.; Wang, D.; Yang, M.; Liang, C. Enhanced hippopotamus optimization algorithm for tuning proportional–integral–derivative controllers. *Front. Inf. Technol. Electron. Eng.* **2025**, *26*, 1356–1377. [CrossRef]
77. Pei, S.; Sun, G.; Tong, L. An improved hippopotamus optimization algorithm based on adaptive development and solution diversity enhancement. *PeerJ Comput. Sci.* **2025**, *11*, e2901. [CrossRef]
78. Talbi, E.-G. (Ed.) *Hybrid Metaheuristics*; Springer: Berlin/Heidelberg, Germany, 2013. [CrossRef]
79. Zhao, F.; Li, Z.; Guo, P.; Zhao, A.; Fu, Y. Enhanced crested porcupine optimizer for numerical optimization and wireless sensor network deployment. *Sci. Rep.* **2025**, *15*, 40141. [CrossRef]
80. Friedman, M. The use of ranks to avoid the assumption of normality implicit in the analysis of variance. *J. Amer. Stat. Assoc.* **1937**, *32*, 675–701. [CrossRef]
81. Iman, R.L.; Davenport, J.M. Approximations of the critical region of the Friedman statistic. *Commun. Stat. Theory Methods* **1980**, *9*, 571–595. [CrossRef]
82. Demšar, J. Statistical comparisons of classifiers over multiple data sets. *J. Mach. Learn. Res.* **2006**, *7*, 1–30.
83. Skillings, J.H.; Mack, G.A. On the use of a Friedman-type statistic in balanced and unbalanced block designs. *Technometrics* **1981**, *23*, 171–177. [CrossRef]
84. Wilcoxon, F. Individual comparisons by ranking methods. *Biom. Bull.* **1945**, *1*, 80–83. [CrossRef]
85. Wilcoxon, F. Probability tables for individual comparisons by ranking methods. *Biometrics* **1947**, *3*, 119–122. [CrossRef]
86. Hollander, M.; Wolfe, D.A.; Chicken, E. *Nonparametric Statistical Methods*, 3rd ed.; Wiley: Hoboken, NJ, USA, 2013.

87. Holm, S. A simple sequentially rejective multiple test procedure. *Scand. J. Stat.* **1979**, *6*, 65–70.
88. García, S.; Herrera, F. An extension on 'Statistical Comparisons of Classifiers over Multiple Data Sets' for all pairwise comparisons. *J. Mach. Learn. Res.* **2008**, *9*, 2677–2694.

Disclaimer/Publisher's Note: The statements, opinions and data contained in all publications are solely those of the individual author(s) and contributor(s) and not of MDPI and/or the editor(s). MDPI and/or the editor(s) disclaim responsibility for any injury to people or property resulting from any ideas, methods, instructions or products referred to in the content.